Fundamental methods to measure the orbital angular momentum of light

---

PROEFSCHRIFT

ter verkrijging van
de graad van Doctor aan de Universiteit Leiden,
op gezag van Rector Magnificus prof. mr. P. F. van der Heijden,
volgens besluit van het College voor Promoties
te verdedigen op dinsdag 20 september 2011
klokke 13.45 uur

door

Gregorius Cornelis Gerardus Berkhout

geboren te Beverwijk, Nederland
in 1983

PROMOTIECOMMISSIE

Promotor:	Prof. dr. M. W. Beijersbergen	cosine Universiteit Leiden
Leden:	Dr. M. P. van Exter	Universiteit Leiden
	Prof. dr. G. W. ’t Hooft	Philips Research Universiteit Leiden
	Prof. dr. M. J. Padgett	University of Glasgow
	Prof. dr. J. P. Woerdman	Universiteit Leiden
	Prof. dr. E. R. Eliel	Universiteit Leiden

An electronic version of this dissertation is available at the Leiden University Repository (https://openaccess.leidenuniv.nl).

ISBN: 978-90-8593-103-4

Casimir PhD series, Delft-Leiden, 2011-14

aan mijn ouders

Contents

1 **Introduction** 1

2 **Probing the orbital angular momentum of light with a multipoint interferometer** 3
- 2.1 Introduction . . . 4
- 2.2 Theory and simulations . . . 5
- 2.3 Experiment and results . . . 8
- 2.4 Discussion . . . 9
- 2.5 Conclusion . . . 11

3 **Using a multipoint interferometer to measure the orbital angular momentum of light** 13
- 3.1 Introduction . . . 14
- 3.2 Characterising interference patterns . . . 18
- 3.3 General optical vortices . . . 19
- 3.4 Conclusion . . . 23

4 **Measuring optical vortices in a speckle pattern using a multi-pinhole interferometer** 25
- 4.1 Introduction . . . 26
- 4.2 Experiment . . . 27
- 4.3 Results . . . 28
- 4.4 Discussion . . . 31
- 4.5 Conclusion . . . 31

5 **Quantitative mapping of the optical vortices in a speckle pattern** 33
- 5.1 Introduction . . . 34
- 5.2 Theory . . . 35
- 5.3 Analysis . . . 38
- 5.4 Experiment . . . 40
- 5.5 Results . . . 41

5.6 Conclusion 41

6 Efficient sorting of orbital angular momentum states of light 45
6.1 Introduction 46
6.2 Theory 46
6.3 Experiment and results 49
6.4 Discussion 52
6.5 Conclusion 52

7 Measuring orbital angular momentum superpositions of light by mode transformation 55
7.1 Introduction 56
7.2 Theory 57
7.3 Experiment 57
7.4 Results 58
7.5 Discussion 60
7.6 Conclusion 60

8 Towards applications based on measuring the orbital angular momentum of light 63
8.1 Introduction 64
8.2 Multi-pinhole interferometer 65
8.3 Mode sorter 72
8.4 Conclusion 76

Bibliography 81

Samenvatting 83

Curriculum Vitae 85

List of publications 87

Nawoord 89

CHAPTER 1

Introduction

Light is a ubiquitous carrier of information. Its intensity, direction, frequency and polarisation provide knowledge about its source and the medium it has propagated through. By means of photodetectors, cameras, spectrometers and polarisers, these properties of light can be measured efficiently. Not only can one obtain knowledge about the source and medium in this way; one can also use light to transfer data from one place to another by encoding this data in one or more properties of the light.

In the past twenty years, great interest has been shown for another property of light, its orbital angular momentum. Contrary to the polarisation, which is associated with the spin angular momentum of light and can take two orthogonal states, the orbital angular momentum can take infinitely many orthogonal states. If this property can be measured efficiently, it opens the way to interesting new physics and could serve as an additional property to encode data in, with its infinitely many possible states as its greatest asset.

The orbital angular momentum of light is associated with Laguerre-Gaussian beams, that contain a phase singularity around which the phase of the field increases in an azimuthal fashion, $\exp(i\ell\phi)$, forming a so-called optical vortex. The intensity vanishes at the position of the singularity, forming a dark hole in the intensity profile of the beam. Each photon in a Laguerre-Gaussian beam carries an orbital angular momentum of $\ell\hbar$. ℓ is often also used to indicate the topological charge of the optical vortex. The case where $\ell = 0$ corresponds to a flat wave front, of which the light coming from a distant point source, for instance a star, is the most common example. Generating beams with an optical vortex is accomplished by special optical elements, such as a spiral phase plate, a fork hologram or a spatial light modulator, that all imprint the azimuthal phase profile to an incoming beam. A wide range of ℓ can be achieved in this way. Optical vortices also occur naturally, for example as higher-order laser modes, in speckle patterns and in optical caustics.

Efficient measurement of the orbital angular momentum of light is very challenging. An ideal measurement system should have infinitely many output ports, each corresponding to a different orbital angular momentum state, much like a polarising beam splitter for measuring the spin angular momentum, which has two output ports, corresponding to each of the two polarisation states. An alternative way to determine the spin angular momentum of a photon is to use a polariser, which transmits one of the states and blocks the other and can be seen as a filter for a specific spin angular momentum state.

Several methods to measure the orbital angular momentum of light have been studied in the past. Interference of a beam containing an optical vortex with a flat wave front results in an interference pattern with a fork-like structure that reveals the topological charge of the vortex. The need for an additional flat wave front make this method unfavourable for many applications, especially when the beam under study is spread out over a large area. A filter for orbital angular momentum states can be achieved with a spiral phase plate, that can be used to test whether the input light is in a specific state or not. Finally, a system of Mach-Zehnder interferometers and Dove prisms provides a measurement of the orbital angular momentum state, but is technically very challenging and difficult to implement in a larger optical system.

In this thesis, we present two new ways to measure the orbital angular momentum of light. The first method, which we describe in detail in chapter 2 and 3, is based on a multi-pinhole interferometer, a system of a number of pinholes arranged on a circle. We demonstrate that by studying the diffraction pattern behind such a multi-pinhole interferometer, one can determine the topological charge of an incoming optical vortex. Since a multi-pinhole interferometer consists of a finite number of apertures, that can be placed far apart, this system can be used to study optical fields with large-scale intensity fluctuations, such as, for instance, can be expected in astronomy. The multi-pinhole interferometer can also be used to make optical vortex maps of an optical field, which makes it possible to not only determine the topological charge of the vortices in the field, but also their anisotropy and orientation. We describe this method and present its results for a speckle pattern in 4 and 5.

In chapter 6, we present the second new way to measure the orbital angular momentum of light, the mode sorter, which approaches the ideal measurement system described before very closely. The mode sorter consists of two custom optical components that transform the azimuthal phase profile of an optical vortex into a tilted plane wave. An additional lens focusses these tilted plane waves to different positions on a detector. These positions are related to the orbital angular momentum of the incoming light. In chapter 7 we demonstrate that this mode sorter can also determine the contribution of each orbital angular momentum state in a superposition. In special cases, we can even determine the relative phase between the modes.

All theory, simulations and experiments presented in chapter 2 to 7, have been performed with monochromatic and fully coherent light. In chapter 8, we theoretically study the response of both the multi-pinhole interferometer and the mode sorter for polychromatic and (partially) incoherent light. The results of these calculations form the starting point for studying applications of measuring the orbital angular momentum of light.

CHAPTER 2

Probing the orbital angular momentum of light with a multipoint interferometer

We present an efficient method for probing the orbital angular momentum of optical vortices of arbitrary sizes. This method, based on a multipoint interferometer, has its most important application in measuring the orbital angular momentum of light from astronomical sources, opening the way to interesting new astrophysics. We demonstrate its viability by measuring the orbital angular momentum of Laguerre-Gaussian laser beams.

G. C. G. Berkhout and M. W. Beijersbergen, *Method for probing the orbital angular momentum of optical vortices in electromagnetic waves from astronomical objects,* Physical Review Letters **101**, 100801 (2008).

2.1 Introduction

It is well understood that light carries angular momentum that, under given circumstances, can be separated into spin and orbital angular momentum [1, 2]. The spin angular momentum is associated with polarization and its transfer to a material body has been measured by Beth [3]. The orbital angular momentum (OAM) is associated with an optical vortex and gives rise to a complex field amplitude of the form $\propto \exp(i\ell\phi)$ and thus a twisted wave front. Such a field has an on-axis singularity resulting in a central dark point in the intensity profile and every photon in it carries an OAM of $\ell\hbar$ [1]. It has been demonstrated that the OAM of a laser beam enables it to rotate trapped particles [4].

Laser beams with OAM occur spontaneously as higher-order transverse modes or can be created using a spiral phase plate (SPP) [5] or a fork hologram (FH) [6, 7]. Optical vortices also occur in speckle patterns [8, 9], where until now only vortices with topological charge -1 and +1 [10] have been observed and higher-order zeros are, although not strictly forbidden, very unlikely.

Recently, the interest for OAM of light in astrophysics has grown [11]. Several possible sources of OAM have been suggested, from bright point sources behind a turbulent interstellar medium to the cosmic microwave background (CMB). Measurement of the OAM of the associated vortices could open the way to interesting new astrophysics. Due to the large propagation distances one expects the intensity variation of astronomical optical vortices to be on very large scales.

Determining the OAM state of an optical vortex requires knowledge of the phase distribution around the singularity. Thidé *et al.* proposed a method for generating and detecting OAM in low-frequency radio beams [12], using an antenna array for coherent measurement of the local field vector in a finite number of points and software to reconstruct the incident vector field. We propose a method based on measuring only the phase instead of the full electric vector, that would allow detection of OAM at optical wavelengths.

Since direct measurement of the phase in the visible regime is not possible, one needs to rely on interferometric techniques. Leach *et al.* [13] proposed an interferometric method for measuring the OAM of a single photon. A more commonly used technique is to interfere the wave front under study with a flat wave front [14, 15], in which case the interferogram reveals the OAM state of the optical vortices. This technique can also be applied to less symmetric optical vortices such as those occurring in speckle patterns, where the interferogram shows their position, OAM state and skewness [8]. In principle, this method allows one to distinguish between infinitely many states.

When the optical vortex is large compared to the detector area, it becomes difficult to measure the phase distribution, since the dark region around the singularity is accordingly larger, leaving less light to interfere with. Moving the detector away from the axis of the vortex towards areas of higher intensity does not solve this, since the amount of phase change over a given area decreases as one moves radially outwards. A possible solution is to use more that one aperture roughly separated by the size of the optical vortex. Performing Young's double slit experiment [16] with Laguerre-Gaussian beams indeed reveals information about the OAM state of the beam [17]. However in this case the length of the slits has to be of the order of the size of the beam, which in many astronomical cases is infeasible.

This problem can be solved by using pointlike apertures instead of slits. In this chapter we describe a system of two or more points, enclosing the singularity of the optical vortex, which we call a multipoint interferometer (MPI), and show that it can be used to measure the OAM state of an optical vortex. We experimentally realize this system by replacing the points with pinholes. This so-called multi-pinhole interferometer has been studied in the context of partially coherent light [18, 19] where the resulting interference patterns reveals information about the coherence properties of the illuminating beam.

2.2 Theory and simulations

We start by studying the proposed method theoretically. The most convenient class of optical vortices are the Laguerre-Gaussian (LG) beams, which have a complex field amplitude given by

$$u_{p\ell}(r,\phi,z) \propto r^{\ell} L_p^{\ell}\left(\frac{2r^2}{w^2}\right)\exp\left(-\frac{r^2}{w^2}\right)\exp(-i\ell\phi), \tag{2.1}$$

where w is the waist size of the beam, $L_p^{\ell}(2r^2/w^2)$ is the associated Laguerre polynomial, p is the radial mode index and ℓ is the azimuthal mode index.

Since the optical vortices are rotationally symmetric in intensity, we choose to uniformly distribute the points in the MPI in a circle, centered around the singularity of the optical vortex. A general MPI consists of N points, has radius a and lies in the xy plane (see figure 2.1).

Since we consider the Fraunhofer limit, the far-field intensity pattern I_{ℓ}^{N} behind a general MPI illuminated by an on-axis, normally incident LG beam is given by the Fourier transform of the field distribution in the aperture plane

$$I_{\ell}^{N}(x,y,z) \propto \left|\sum_{n=0}^{N-1} \exp\left(-i\ell\alpha_n\right)\exp\left(i\frac{ka}{z}\left(x\cos\alpha_n + y\sin\alpha_n\right)\right)\right|^2, \tag{2.2}$$

where $k = 2\pi/\lambda$ is the wave number and $\alpha_n = 2\pi n/N$ the azimuthal coordinate of the nth point. For two pinholes and a Gaussian beam (i.e., $\ell = 0$), equation 2.2 reduces to $I_0^2 \propto \cos^2(kax/z)$, reproducing the result for the central part of the interference pattern in Young's experiment with two pinholes. If the number of points goes to infinity, corresponding to an annular aperture, equation 2.2 converges to the Bessel function of the first kind of order $|\ell|$, $J_{|\ell|}(kar/z)$, where r is the radial distance. For other values of N and ℓ, equation 2.2 yields unexpectedly complex patterns, some of which are shown in figure

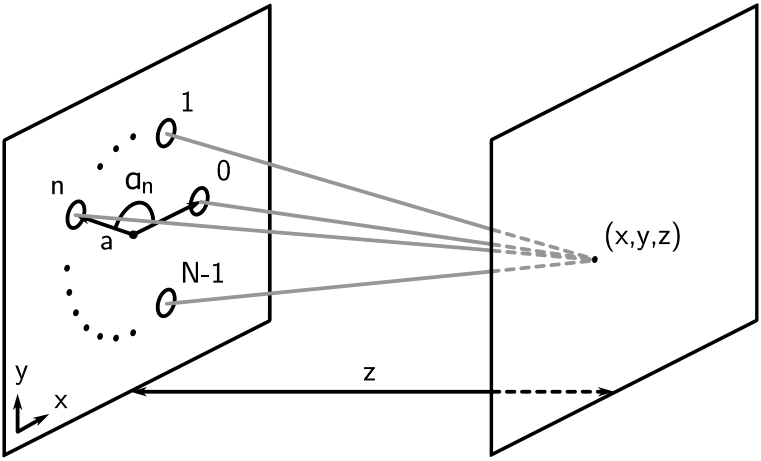

Figure 2.1: Geometry and notation of a generic multipoint interferometer consisting of N points, uniformly distributed over a circle of radius a in the xy plane. The points are indicated by open dots and the angular coordinate of the nth point is $\alpha_n = 2\pi n/N$.

2.2.

A nonzero azimuthal mode index has a significant effect on the observed patterns, as can be seen by comparing the second and third column of figure 2.2 to the first. The results for $N = 2$ are easily understood; the azimuthal phase dependence of the LG beam introduces a phase difference of π between the two points for odd ℓ, shifting the observed patterns by half a period with respect to the patterns for even ℓ. This phase difference can however also be introduced by a tilt of the illuminating beam with respect to the plane of the MPI, making it impossible to distinguish between OAM and a tilt of the beam. The same arguments hold for $N = 3$ where we observe three shifted patterns that repeat for $\ell' = \ell + 3$. A two or three point interferometer can therefore only be used to measure the OAM if the optical axis of the illuminating beam is known.

This ambiguity is however removed in the case of four or more points, where the phase distribution caused by different values of ℓ is inherently different from the phase differences introduced by a tilt of the incoming wave front. This can be seen from simple geometry, and it is also evident in the resulting patterns. For four points some ℓ states result in a shift of the pattern but, more importantly, others in qualitatively different patterns. Even though the patterns for five points look similar by eye, all patterns in this case differ significantly, in particular in the details surrounding the bright spots. Further simulations show that for an MPI of N points we observe N different patterns. The patterns for positive and negative ℓ are mirrored in the x axis (see figure 2.3). For an even number of points the patterns are symmetric in the x axis and in this case there is no difference between the pattern for positive and negative ℓ, making it impossible to differentiate between negative and positive OAM states, reducing the number of distinguishable states

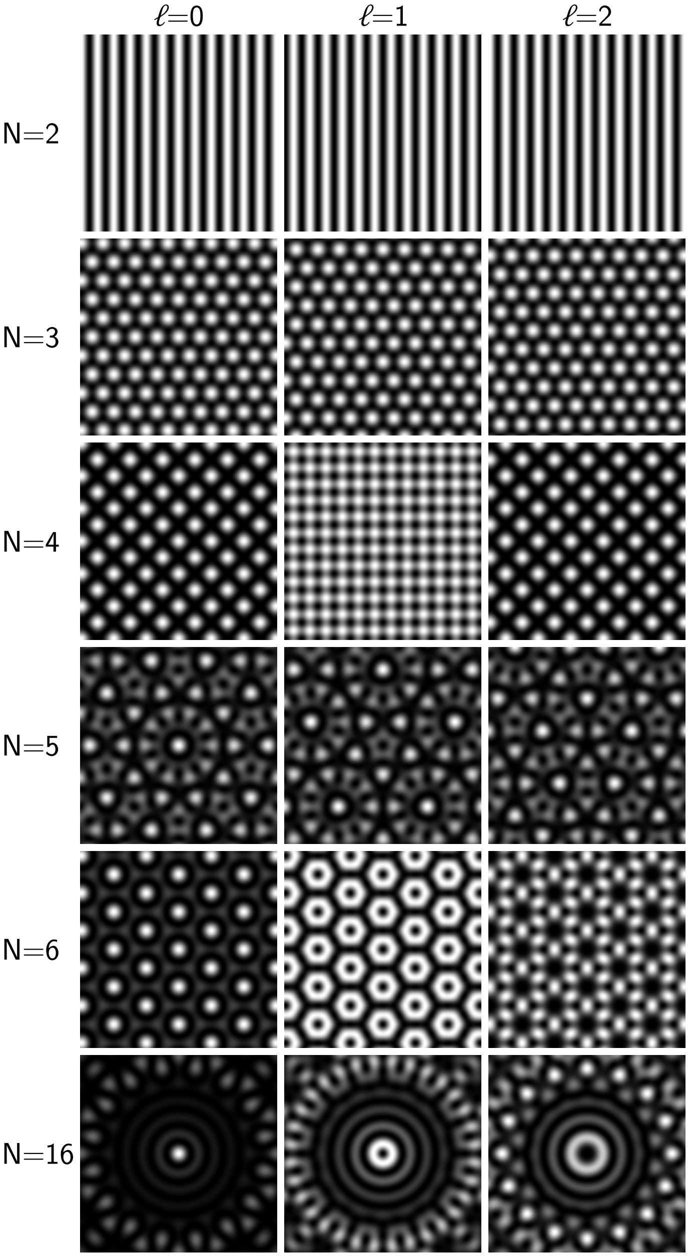

Figure 2.2: Far-field intensity patterns behind an MPI of N points illuminated by an LG beam with azimuthal mode index ℓ calculated from equation 2.2 (linear gray scale, white corresponds to high intensity). $N = 2$, $\ell = 0$ reproduces the results for Young's experiment with two pinholes. $N = 16$ hints at the fact that the observed patterns converge to a Bessel function of order $|\ell|$. At intermediate values the pattern is very dependent on the azimuthal mode index ℓ, and therefore the OAM of the field at the location of the MPI.

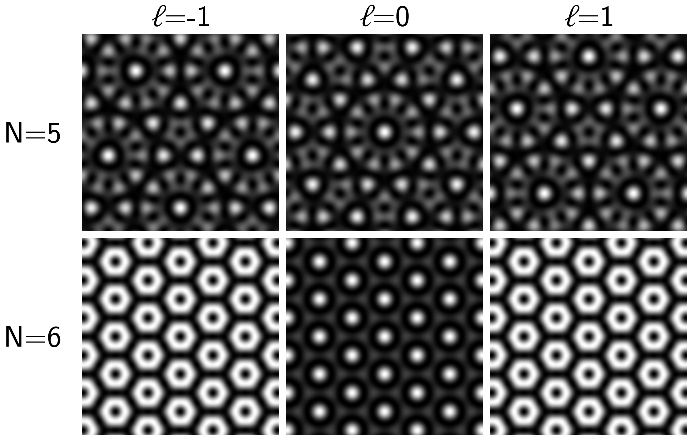

Figure 2.3: Simulated far-field intensity patterns behind an MPI of N points illuminated by an LG beam with azimuthal mode index ℓ calculated from equation 2.2. The patterns for ℓ values of opposite sign are mirrored in the x axis. For an odd number of points one can determine the sign of ℓ.

to $N/2 - 1$.

Further simulations have shown that the observed qualitative patterns change only marginally when the phase front is not perpendicular to the interferometer plane, proving that an MPI is an efficient OAM detector if it consists of at least four points.

2.3 Experiment and results

To demonstrate the method we measured the interference patterns behind a multi-pinhole interferometer, where the diffraction of the light on the pinholes is used to overlap the light from the different points. We assume that the finite size of the pinholes does not change the interference pattern qualitatively, but adds a convolution with the diffraction pattern of a single pinhole to it. The size of the multi-pinhole interferometer is chosen to be of the order of the waist size of the beam in order to collect maximum intensity from the donut-shaped intensity profile of an $\ell = 1$ laser beam.

We built a setup to study the interference patterns (see figure 2.4 for details) and measured the interference pattern for the different multi-pinhole interferometers for ℓ between -3 and $+3$. All observed patterns show excellent agreement with the simulations as can be seen by comparing figures 2.2 and 2.5. The effect of the finite size of the pinholes can be seen at the edges of the patterns where the intensity drops.

Even if the LG beam is not perfectly on-axis and perpendicular, the observed pattern can still be distinguished clearly, as long as the singularity is located within the circle formed by the pinholes. For example in figure 2.5, the observed pattern for $N = 4$, $\ell = 1$ is skewed but can still be clearly differentiated from $\ell = 0$ and $\ell = 2$.

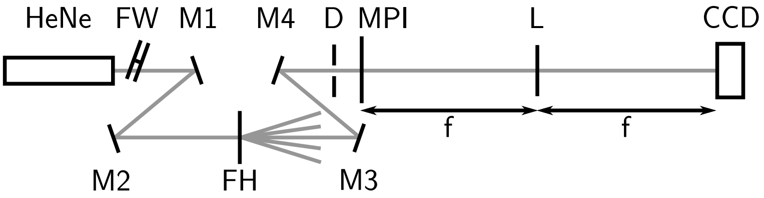

Figure 2.4: Setup to measure interference patterns behind a multi-pinhole interferometer. A helium-neon laser (HeNe), a filter wheel (FW), two mirrors (M1 and M2) and a fork hologram (FH) are used to create LG beams and a set of mirrors (M3 and M4) and a diaphragm (D) are used to select an LG beam to illuminate the multi-pinhole interferometer (MPI). A CCD camera (CCD) and a lens (L) are used to record the far-field image.

2.4 Discussion

We demonstrated that the interference pattern behind an MPI illuminated by an LG beam yields information about the azimuthal mode index ℓ of the beam. To our knowledge this is the first method that can be used to measure the OAM of light, without requiring coverage of a large area of the field. As our detection method relies only on a finite number of point measurements, it can be scaled to arbitrarily large sizes and can thus be used to measure arbitrarily large optical vortices such as expected to come from astronomical sources. In the experiments that we performed, we used the diffraction of light on small pinholes to overlap the light from the different points. With this method, the position of the far field increases with increasing separation of the points, leading to increasingly large system size, and increasingly small periodicity of the patterns, making it more difficult to detect. In order to increase the size of the MPI, extra measures have to be taken to combine the light, for example using telescopes and mirrors. This is what is foreseen in the Darwin mission [20]. Darwin is a space-based infrared nulling interferometer that combines the light from four telescope satellites in a central beam combiner satellite. As the telescopes are small with respect to the distance between them, the system operates as a multi-pinhole interferometer. The light from the different telescopes follows paths of equal length to the beam combiner. In fact, the nulling in Darwin is obtained by introducing phase shifts between the telescopes that correspond to a $\ell = 1$ mode, converting an incoming plane wave into a vortex with a null in the center. This is essentially the same as is done in a vortex coronagraph [21], effectively making Darwin a synthetic aperture version of a vortex coronograph. Darwin would be a perfect detector for astronomical OAM at length scales of hundreds of meters, provided that the different interference patterns can be distinguished. The technique of multipoint interferometry can also be implemented in other existing and future telescope arrays, such as the the VLT [22], ALMA [23] and KEOPS [24], albeit slightly modified because of the noncircular arrangement of the individual telescopes.

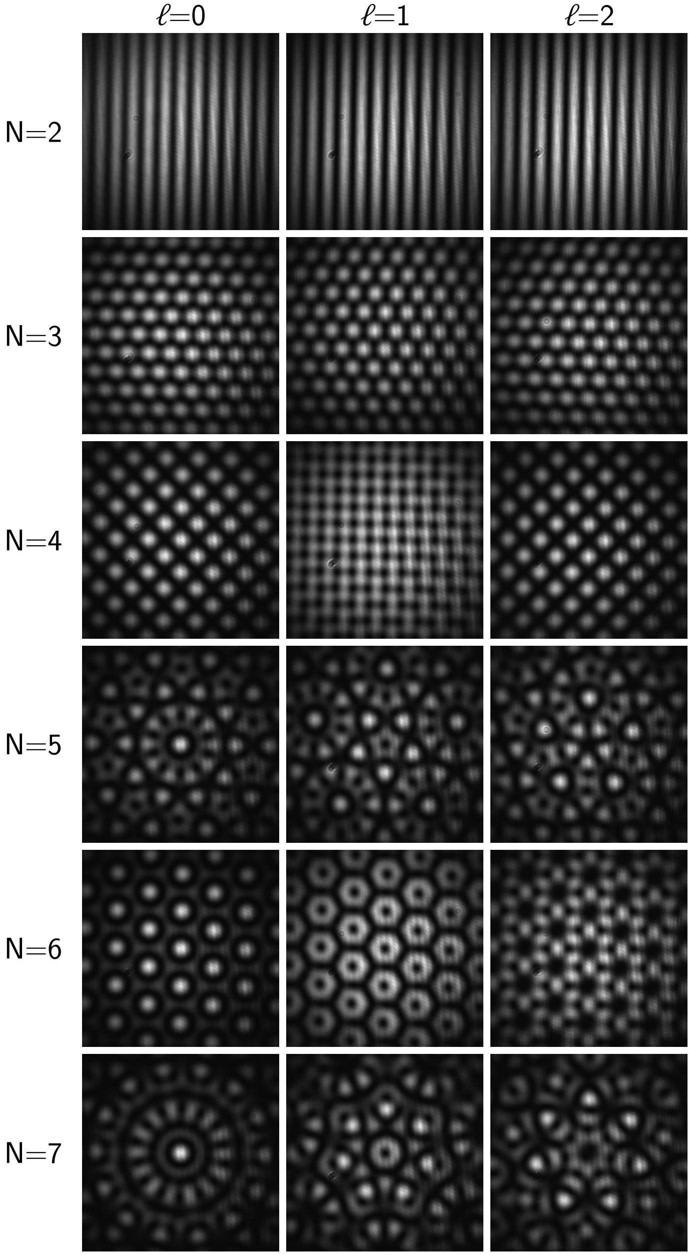

Figure 2.5: Measured far-field intensity patterns behind an MPI of N points illuminated by an LG beam with azimuthal mode index ℓ. The measured patterns show excellent agreement with the calculated ones (compare figure 2.2).

2.5 Conclusion

In conclusion, we discussed a new interferometric technique to probe the OAM of light. This technique uses an MPI which makes use of the interferometric combination of the light from a finite number of point measurements. This allows to scan a field for phase singularities and measure their corresponding OAM of light, does not require knowledge of the direction of the beam, and can be scaled to arbitrary dimensions because it samples only a finite number of points in the field. This scalability makes the detection method very useful for systems where the optical vortices are expected to be large, such as in astrophysics. Multi-telescope systems can be used as OAM detectors provided that at least four telescopes are used.

CHAPTER 3

Using a multipoint interferometer to measure the orbital angular momentum of light

Recently it was shown that the orbital angular momentum of light can be measured using a multipoint interferometer, a system in which the light from several point measurements is interferometrically combined. This system has important applications in optics but could also be employed to detect astrophysical orbital angular momentum. Until now, the response of a multipoint interferometer to an on-axis, normally incident Laguerre-Gaussian beam has been studied by visual inspection. In this paper we present an algorithm to determine the orbital angular momentum of the impinging beam from the obtained interference patterns. Using this algorithm we extend our study to general optical vortices and a superposition of optical vortices.

G. C. G. Berkhout and M. W. Beijersbergen, *Using a multipoint interferometer to measure the orbital angular momentum of light in astrophysics,* Journal of Optics A: Pure and Applied Optics **11**, 094021 (2009).

3.1 Introduction

Since its discovery, the orbital angular momentum (OAM) of light has been studied intensively [1, 25]. The fact that light carries angular momentum that, under given circumstances, can be separated into spin and orbital angular momentum is nowadays well known. Recently the possibility that light from astronomical sources possesses OAM was suggested [11, 26]. Detection of this OAM may have interesting implications for astrophysics, since it is known that the OAM of light can be transferred to small particles or atoms (for a recent review, see [25]). A method for detecting OAM in low-frequency radio beams has been proposed recently [12]. Since this method relies on a coherent measurement of the local field vector it cannot be applied to optical wavelengths. In this paper we describe the details of the method that was proposed in [27], based on a so-called multipoint interferometer. The main advantage of this method lies in the fact that it relies on only a finite number of point measurements, making it possible to measure OAM on, in principle, arbitrarily large length scales.

The simplest class of light fields carrying OAM are the so-called optical vortices. A general optical vortex has a complex field amplitude of the form $\propto \exp(i\ell\phi)$, resulting in a phase singularity at its centre. At the position of this phase singularity, the intensity drops to zero. As one makes a full turn around the singularity in counterclockwise fashion, the phase increases by $2\pi\ell$, where ℓ is the vorticity. Away from the singularity the intensity increases until, for an isolated optical vortex, it consequently drops outside a bright ring of radius proportional to ℓ. The exact form of the intensity profile depends on the origin and propagation of the optical vortex and the presence of other optical vortices. Optical vortices can be created, for example, using a spiral phase plate [5] or a fork hologram [6, 7], but they also occur in more generic fields, such as in speckle patterns [8, 28].

Several methods exist to detect optical vortices. A method that is often used is interfering the optical vortex with a flat wave front. The resulting interference pattern reveals information on the vorticity, the position and the anisotropy of the optical vortex [8]. One can also convert an optical vortex to a Gaussian beam using holographic techniques and detect its intensity using a monomode fibre or pinhole [29]. Both methods require the coveragd of an extended region around the optical vortex in order to detect the vorticity.

So far no quantitative analyses of the expected optical vortices from astronomical sources have been presented. The only reasonable assumption one can make is that the associated intensity profile will fluctuate on large scales due to the large propagation distances of the light coming from these sources. It will therefore be virtually impossible to cover a sufficient part of the intensity profile using a single detector, making it impossible to measure the vorticity using interference with a flat wave front. This is illustrated by figure 3.1. One can place the detector near the centre of the optical vortex where the phase varies rapidly, but the amplitude is very low. Alternatively one can place the detector in regions of higher intensity, but hardly any phase change is present there. In a

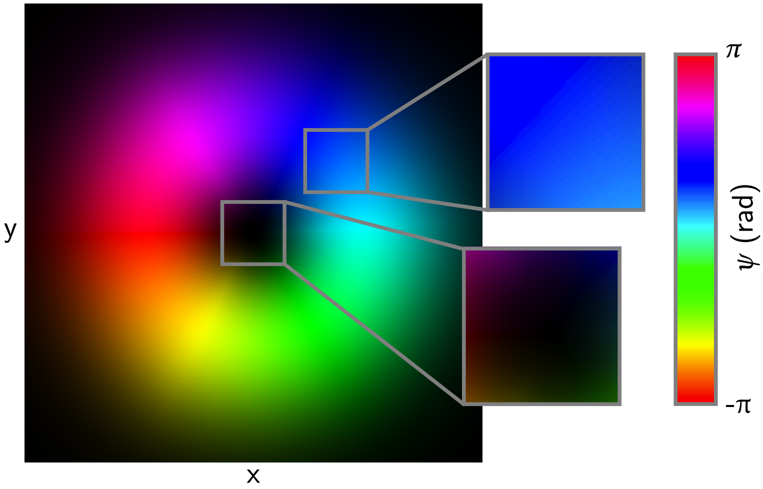

Figure 3.1: A Laguerre-Gaussian $\ell = 1$ beam (see text for details). Colours indicate phase, while intensity shows amplitude. This figure shows the intrinsic difficulty in measuring the orbital angular momentum of light if only a small part of the beam can be covered using a single detector (shown as grey squares). In the centre there is hardly any intensity, while in the outer parts there is hardly any phase change.

previous paper [27] we discussed an interferometric method based on a so-called multipoint interferometer, where the light of several points, roughly separated by the typical length scale of the intensity fluctuations around the optical vortex, is interferometrically combined. From the resulting interference patterns the vorticity of the impinging vortex can be determined. We experimentally realised the multipoint interferometer by a multi-pinhole interferometer, where we used the diffraction of the light at the pinholes to overlap the light from the different points. Theory and experiment using laser beams prove to be in excellent agreement.

It is possible to scale a multipoint interferometer to, in principle, arbitrary sizes by replacing the pinholes by telescopes and using beam combiner optics to interferometrically combine the light from the different telescopes. This technique could already be implemented at existing telescope arrays, where one has to take into account the non-circular arrangement of the telescopes.

A convenient basis for describing a light beam possessing OAM are the Laguerre-Gaussian beams which have a complex field amplitude given by

$$u_{p\ell}(r,\phi,z) \propto r^{\ell} L_p^{\ell}\left(\frac{2r^2}{w^2}\right) exp\left(-\frac{r^2}{w^2}\right) \exp(-i\ell\phi), \tag{3.1}$$

where w is the waist size of the beam, $L_p^{\ell}(2r^2/w^2)$ is the associated Laguerre polynomial, p is the radial mode index and ℓ is the vorticity.

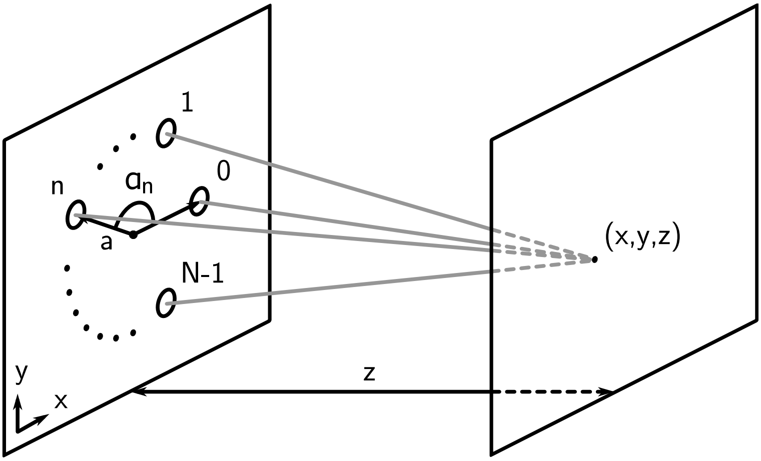

Figure 3.2: Geometry and notation of a generic multipoint interferometer consisting of N points, uniformly distributed over a circle of radius a in the xy plane. The points are indicated by open dots and the angular coordinate of the n-th point is $\alpha_n = 2\pi n/N$.

A general multipoint interferometer consists of N points, uniformly distributed over a circle of radius a as shown in figure 3.2. The azimuthal angle of each point is given by $\alpha_n = 2\pi n/N$. The far-field interference pattern behind a general multipoint interferometer is given by the Fourier transform of the field distribution in the aperture plane. In the case of an on-axis, normally incident Laguerre-Gaussian beam, the interference pattern is given by

$$I_\ell^N(x,y,z) \propto \left|\sum_{n=0}^{N-1} \exp\left(-i\ell\alpha_n\right)\exp\left(i\frac{ka}{z}\left(x\cos\alpha_n + y\sin\alpha_n\right)\right)\right|^2. \tag{3.2}$$

Results of this equation are shown in [27] and in figures 3.3 and 3.4.

In any real system the points will be replaced by apertures and the observed interference pattern will be convoluted by the diffraction pattern of an individual aperture. As long as the diameter of the aperture is small compared to the separation of the apertures, the interference pattern can be observed in the central lobe of the diffraction pattern.

Equation 3.2 gives the interesting result that the interference pattern behind a multipoint interferometer of N points is the same for an impinging beam with $\ell = m$ and $\ell' = m + N$ for $N \geq 4$. This effect can be explained by comparing the phases of the impinging fields at the different points for both ℓ states. The number of distinguishable l states is therefore equal to N and the observed patterns are periodic in ℓ.

It is also observed that the patterns for $\ell = -|m|$ and $\ell = |m|$ are the same but mirrored in the x axis. For an even number of points N, the observed interference patterns are symmetric about the x axis and it is in this case impossible to distinguish between $\ell =$

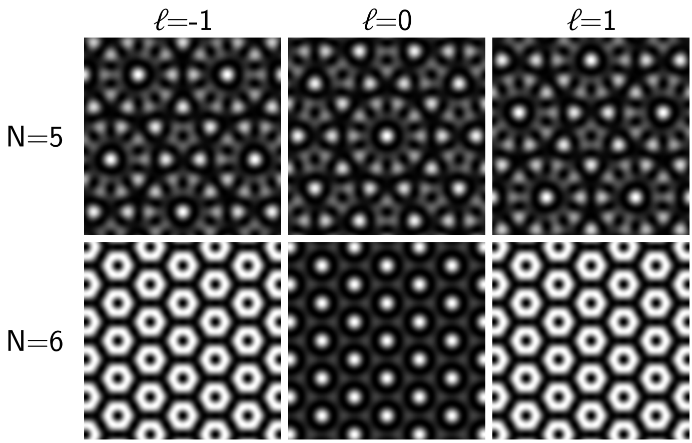

Figure 3.3: Far-field intensity patterns behind an multipoint interferometer of N points illuminated by a Laguerre-Gaussian beam with vorticity ℓ, calculated from equation 3.2. The patterns for $\ell = -|m_\perp|$ and $\ell = |m_\perp|$ are mirrored in the x axis. For an odd number of points N, one can differentiate between the patterns for even and odd values of ℓ; for even N one cannot.

$-|m_\perp|$ and $\ell = |m_\perp|$, reducing the number of distinguishable ℓ states to $N/2 + 1$. Figure 3.3 shows this behaviour for $N = 5$ and $N = 6$. This behaviour is already explained in [27], but is shown here for the sake of completeness.

In a real application one has to take these effects into account in selecting the number of points. It is for instance known that in all observed speckle patterns only optical vortices with $\ell = -1$ and $\ell = 1$ occur [8]. In this case a multipoint interferometer with $N = 5$ would suffices.

For a large number of points N, the multipoint interferometer converges to an annular aperture and the resulting interference pattern is described by the well know Bessel function. The order of the Bessel function depends on the l state of the impinging Laguerre-Gaussian beam since

$$\lim_{N\to\infty} I_\ell^N(x,y,z) \propto \mathcal{J}_{|\ell|}\left(\frac{kar}{z}\right). \tag{3.3}$$

In this limit one cannot distinguish between clockwise and counterclockwise vortices of the same vorticity. Figure 3.4 illustrates that the convergence can already be seen for relatively small number of points, in this case $N = 16$.

So far we have only considered the response to an on-axis, normally incident Laguerre-Gaussian beams, studied by visual inspection. In this paper we will describe an algorithm that can be used to determine the vorticity based on the interference patterns. Using this algorithm we will generalise our findings to general optical vortices.

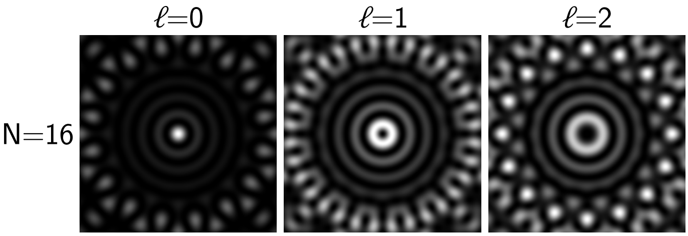

Figure 3.4: Far-field intensity patterns behind an multipoint interferometer of $N = 16$ points illuminated by a Laguerre-Gaussian beam with vorticity ℓ. The intensity patterns hint at the fact that the patterns converge to a Bessel function in the limit that $N \to \infty$ as described by equation 3.3.

3.2 Characterising interference patterns

A general optical field can be decomposed on a bases of Laguerre-Gaussian beams, see e.g. [30]

$$u(r, \phi, z) \propto \sum_{\ell=-\infty}^{\infty} c_\ell u_{p\ell}(r, \phi, z), \tag{3.4}$$

where c_ℓ is a weighting coefficient and $u_{pl}(r, \phi, z)$ are the pure Laguerre-Gaussian modes as described by equation 3.1. As it turns out from the simulations, the interference pattern behind a general multipoint interferometer for this general wave front can be described by

$$I^N = \sum_{\ell=m}^{N+m-1} c_\ell I_\ell^N, \tag{3.5}$$

where m indicates an arbitrary integer and I_ℓ^N are the interference patterns behind a general multipoint interferometer for a pure Laguerre-Gaussian mode as described by equation 3.2. Note that the summation runs over N terms only since the interference patterns for $\ell = m$ and $\ell = m + N$ are the same and hence we can only distinguish N different c_ℓ. In case N is even the summation runs over $N/2 + 1$ terms only. m can be chosen arbitrarily since the interference patterns are periodic in ℓ. The surprising fact is that the intensity patterns form an orthogonal basis for describing the interference patterns.

In practise the weighting constants c_ℓ can be found by performing a 2D convolution algorithm to the interference patterns calculated by

$$c_\ell = I^N * * I_\ell^N(0, 0) = \mathcal{F}^{-1}\left\{\mathcal{F}\left\{I^N\right\} * \mathcal{F}\left\{I_\ell^N\right\}\right\}(0, 0), \tag{3.6}$$

where $**$ denotes convolution, $\mathcal{F}$ and $\mathcal{F}^{-1}$ 2D Fourier transform and 2D inverse Fourier transform respectively and $(0, 0)$ the central pixel of the convolution. In the following analyses this algorithm is used to determine the weighting factors c_ℓ. This algorithm requires knowledge of the response of a multipoint interferometer, but as can be seen in equation 3.2 this response is determined by the number of points and the separation of the pinholes only. For any real optical system the diffraction of the light at the apertures has to be taken into account, but as stated above this will only introduce an envelope on the observed interference pattern.

3.3 General optical vortices

3.3.1 Tilt

In general the singularity axis of an impinging optical vortex will not coincide with the axis of to the multipoint interferometer, which will have an effect on the observed interference patterns. We have studied the effect of a tilt of the optical vortex with respect to the multipoint interferometer.

As can be seen from figure 3.5, a tilt of the impinging optical vortex results in a shift of the observed interference patterns, as is expected since these are far-field interference patterns. In order to determine the vorticity of the optical vortex one first has to shift the pattern to remove the shift introduced by the tilt. This is possible since the centre of the interference pattern is unique for $N \geq 5$, except for $N = 6$. For $N = 4$ and $N = 6$, the centre of the pattern is not uniquely determined but centring at any of the repeating unit patterns will work in this case. In the case of a real detection system, the observed interference pattern is convoluted by the diffraction pattern of a single aperture, which makes it more difficult to find the centre of the interference pattern. Before applying the algorithm described above, one has to make sure that there are enough periods of the interference pattern in the central lobe of the diffraction pattern.

3.3.2 Displacement

A displacement of the beam with respect to the multipoint interferometer results in a blurring of the observed interference patterns as can be seen in figure 3.6. The displacement is quantified by a vector $\mathbf{r}_0 = (x_0, y_0, 0)$. In order to analyse these blurred patterns we use the algorithm that is described above to determine the coefficients c_ℓ. In the simulations we capture only a finite part of the infinite interference patterns, which introduces a certain amount of error in the values c_ℓ. For consistency with the previous part of this paper, we choose the same pinhole separation as used above. However, we note that the error in the determination of c_ℓ can be minimised by increasing the pinhole separation.

We calculated the normalised overlap with the different modes for a optical vortex that is displaced over $\mathbf{r}_0 = (x_0, 0, 0)$. To avoid effects coming from the intensity profile of the optical vortex, we only consider the phase of the optical vortex and set the intensity to be uniform. As explained before the intensity fluctuations for large optical vortices are expected to be on large scales and the intensity between the different points or apertures will not vary much. The results are shown in figure 3.7. As expected, for an on-axis beam, the coefficient c_ℓ equals one for $\ell = 1$ and is zero elsewhere. As the beam is displaced,

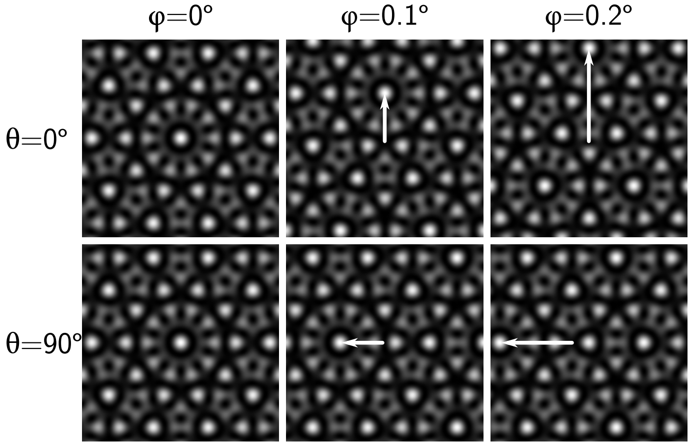

Figure 3.5: Far-field intensity patterns behind an multipoint interferometer of $N = 5$ illuminated by a Laguerre-Gaussian beam with vorticity ℓ. The propagation axis of the impinging beam is tilted with respect to the normal of the multipoint interferometer over θ and ϕ, which are the azimuthal and polar angles respectively. The tilt results in a shift of the observed interference pattern as is indicated by the white arrows.

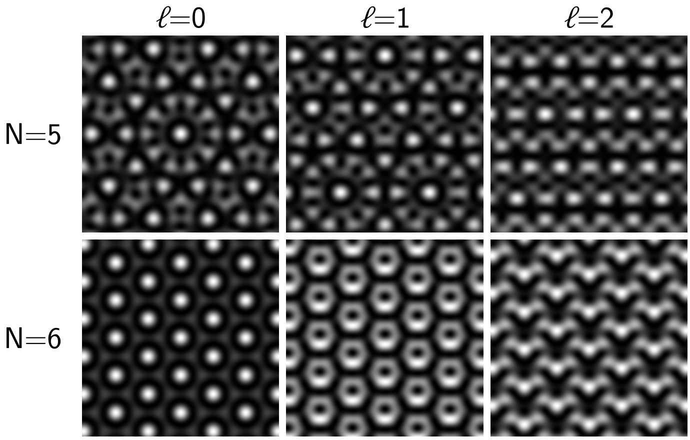

Figure 3.6: Far-field interference patterns behind a multipoint interferometer with $N = 5$ illuminated by an optical vortex of uniform intensity with its centre displaced over $\mathbf{r}_0 = (0.5a, 0, 0)$. The displacement results in a blurring of the interference patterns.

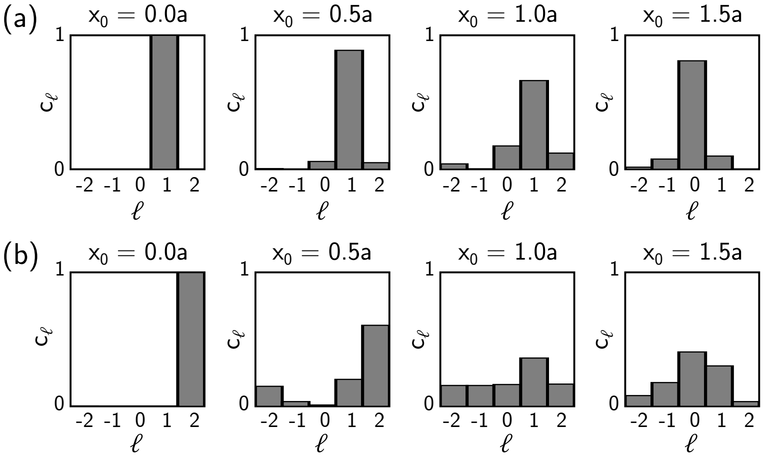

Figure 3.7: (a) Decomposition (see equations 3.5 and 3.6) for a displaced optical vortex with uniform intensity and vorticity $\ell = 1$. The position of the singularity is displaced over distance $\mathbf{r}_0 = (x_0, 0, 0)$. In the limit that the singularity is far from the multipoint interferometer, the wave front that is sensed by the multipoint interferometer becomes essentially flat. (b) Same calculation, but for an optical vortex with $\ell = 2$.

the distribution broadens, but still peaks at $\ell = 1$ of the impinging optical vortex. For even larger displacements there is more and more overlap with the $\ell = 0$ state. Once the singularity moves out of the circle transcribing the pinholes, the $\ell = 0$ component dominates. Further simulations show that this switching behaviour happens very fast. The fact that the distribution converges to a pure $\ell = 0$ state can intuitively be understood, since the wave front that is sensed by the multipoint interferometer effectively becomes flat as the singularity is far away from the centre of the multipoint interferometer.

For an impinging optical vortex with $\ell = 2$, we observe the same behaviour, but in two steps. The resulting interference pattern first shows a strong peak at $\ell = 1$ mode before it finally converges to an $\ell = 0$ state. These simulations confirm the fact it is possible to determine the vorticity of an optical vortex as long as the singularity axis is within the circle through the points of the multipoint interferometer.

3.3.3 Anisotropic optical vortices

Many optical vortices that occur in more generic systems, for instance speckle patterns, are anisotropic, meaning that the phase does not increase linearly with the azimuthal angle around the phase singularity (see figure 3.8). These anisotropic optical vortices can be described by a set of Stokes parameters, using a single parameter α to describe the anisotropy [31, 32] where $0 \leq \alpha \leq \pi$. We analysed the performance of the multipoint interferometer impinged by an anisotropic optical vortex for varying α in terms of its decomposition on the different pure modes. In the simulations we used the same pa-

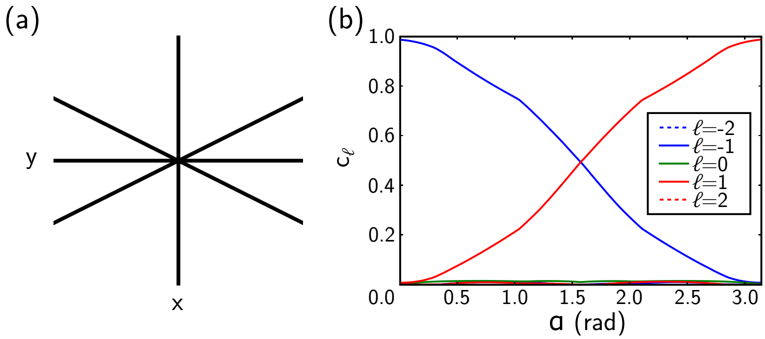

Figure 3.8: (a) Phase profile of an anisotropic optical vortex. The color coding is the same as in figure 3.1. Lines indicate phase contours separated by $\pi/4$. (b) Mode decomposition as a function of α obtained by applying the algorithm as described by equation 3.6.

rameters as above and again only consider the phase of the optical vortex and assume a uniform intensity. One can see that the system is able to determine the vorticity of the impinging beam, except in the region around $\alpha = \pi/2$ where the vortex reduces to an edge dislocation and the vorticity is not defined. The width of the region in which the vorticity is determined is dependent on the experimental error and depends on the real application. As before we note that the error is strongly dependent on the distance between the points, and that the simulations are not optimised for reducing the error. One can see that the vortex changes sign as the anisotropy goes through $\alpha = \pi/2$ since the orientation of the zero field lines of the real and imaginary part changes sign here.

3.3.4 Superposition of optical vortices

It is possible to generate a superposition of Laguerre-Gaussian beams using, for instance, a fork hologram [29, 33]. For communication purposes it would be interesting to be able to decompose this superposition on a basis of pure modes. A general superposition is described by equation 3.5. As described above one can use only N different pure modes when using a multipoint interferometer of N points. Figure 3.9 (a) shows the interference pattern for behind a multipoint interferometer with $N = 5$ for a randomly chosen set of superposition coefficients shown in figure 3.9 (b) as input. Figure 3.9 (b) also shows the output coefficients c_ℓ determined using the algorithm described above. The difference between the input and output values is caused by fact that there is some error in the output coefficients c_ℓ because of the fact that only a finite part of the interference pattern is captured. This can be improved by capturing a larger part of the pattern, for instance by increasing the separation between the points in the multipoint interferometer. This parameter has not been optimised in these simulations.

These simulations show that it is possible to decompose a superposition of optical vortices with different ℓ modes onto a basis of pure ℓ modes using a multipoint interfer-

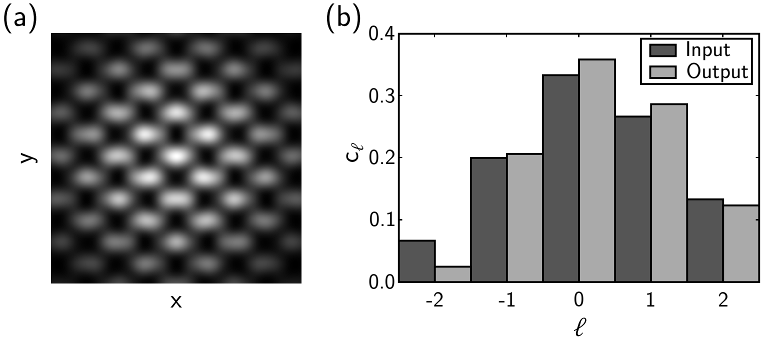

Figure 3.9: (a) Far-field interference pattern behind a multipoint interferometer with $N = 5$ illuminated by a randomly chosen superposition of Laguerre-Gaussian modes. (b) Input randomly chosen superposition coefficients c_ℓ versus output coefficients as determined by using the method described above.

ometer. It requires however several Fourier transforms to perform this decomposition, which cost valuable computation time, making it not very useful for fast communication purposes as opposed to the method proposed by [33] that returns the coefficients c_ℓ without calculation. The multipoint interferometer can however be useful in cases where the beam is strongly diverging, which might occur in long range communication.

3.4 Conclusion

We described an algorithm to characterise the response of a multipoint interferometer and used it to study this response in the case of a general optical vortex and a superposition of optical vortices. This showed that in most cases it is possible to measure the vorticity of the optical vortex. We also showed that a multipoint interferometer can be used to decompose a superposition of Laguerre-Gaussian modes, which is potentially useful for application in free space communication, albeit that the analysis is time consuming. We conclude that a multipoint interferometer is a useful tool for measuring the vorticity of a general vortex of, in principle, arbitrary sizes as are expected to be associated with OAM in astrophysics.

CHAPTER 4

Measuring optical vortices in a speckle pattern using a multi-pinhole interferometer

We show that it is possible to find and characterise optical vortices in a speckle pattern using a multi-pinhole interferometer. This measurement does not require an additional flat wave front to interfere with the speckle, providing great experimental ease. In addition, a multi-pinhole interferometer can be made arbitrarily large and can therefore be adjusted to the expected speckle size. We present experimental results confirming our understanding.

G. C. G. Berkhout and M. W. Beijersbergen, *Measuring optical vortices in a speckle pattern using a multi-pinhole interferometer,* Optics Express **18**, 13836 (2010).

4.1 Introduction

Speckle patterns are very common in optics, since they occur when coherent light is scattered by a rough surface or an inhomogeneous medium [34]. The rough texture of the surface or medium causes the scattered light to interfere in a random fashion resulting in the well-known granular far-field intensity patterns.

The theory of speckle is well established [35]. Due to the random nature of the interference, points exist in a speckle pattern where the field amplitude is equal to zero and the phase is singular. Around these singular points, the field is proportional to $\exp(i\ell\phi)$, or, in other words, the phase varies in an azimuthal fashion, forming an optical vortex [10]. Optical vortices are generally associated with orbital angular momentum [1]. Many experimental and theoretical studies have been performed on the optical vortices in speckle patterns [8, 28, 30, 36–38]. Optical vortices in speckle mostly have topological charge ± 1, however very rare doubly degenerate vortices have been observed [36]. Contrary to the optical vortices in Laguerre-Gaussian beams, the vortices in speckle patterns are anisotropic, meaning that the phase of the field does not increase linearly with the azimuthal angle around the singularity [9, 32]. The phase distribution in speckle patterns may be studied experimentally by interfering the pattern with a flat wave front [8]. The position of the vortex shows up as a fork-like structure in the interference pattern with its topological charge given by the orientation of the fork.

Recently it was suggested that light from astronomical sources could posses orbital angular momentum [11, 26, 39, 40]. One of the most likely fields to contain this orbital angular momentum is a speckle pattern caused by starlight scattering from a inhomogeneous interstellar medium [11]. Studying these patterns could reveal interesting new information about the star and the interstellar medium. Because of the large distance between the scatterer and the detector, these speckles are expected to be large compared to available detectors, making it impossible to study them by interference with a flat wave front.

We recently studied an alternative way to find and characterise optical vortices, that is based on measuring and analysing the interference pattern behind a multipoint interferometer, which consists of a finite number of small apertures arranged in circular fashion [27]. We showed that the interference pattern contains information on the vorticity of the optical vortex impinging the apertures. Guo et al. [41] developed an efficient analysis to extract the relative phases of the light at the individual apertures by performing a Fourier transform on a single interference pattern. Because the system is based on a finite number of pinholes, the light throughput is inherently not very high, making it less suitable for applications at low light levels. In this paper we demonstrate experimentally that the multi-pinhole interferometer, in combination with the Fourier transform method to analyse the interference pattern, can be used to measure vorticity in a speckle pattern, opening the way to do this on a variety of sources including astronomical.

To demonstrate this method experimentally, we measured optical vortices in the lab-

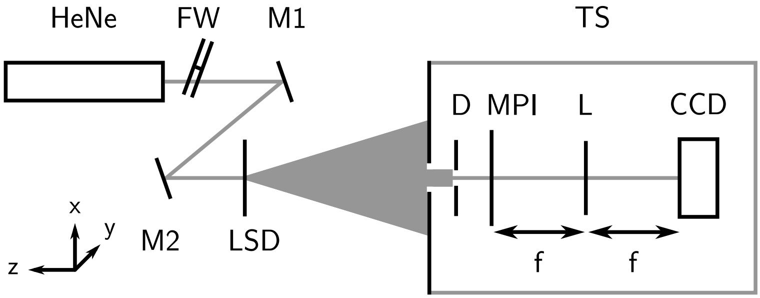

Figure 4.1: Schematic drawing of the setup that is used to measure optical vortices in a speckle pattern. A helium-neon laser (HeNe), appropriately attenuated with a neutral density filter wheel (FW), and two mirrors (M1 and M2) are used to illuminate a small part of a light shaping diffusor (LSD) which creates the speckle pattern. At a sufficiently large distance to guarantee fully developed speckle, a multi-pinhole interferometer (MPI), a lens (L) and a CCD camera (CCD) are placed on a translation stage (TS) that can be moved in the x and y-direction. Several multi-pinhole interferometers with different number of pinholes, pinhole separation and pinhole diameter are combined on a single optical component and a diaphragm (D) is used to select one.

oratory using pinholes, forming a multi-pinhole interferometer [42]. One could also think of replacing the points by telescopes and using recombination optics to overlap the light from the different points. In principle, any given point separation would be possible in this way, making it also suitable for the case that the speckle is much larger than a single detector. We proved theoretically that this method is sensitive to detect anisotropic optical vortices and found that the vortex can be identified as long as the singularity is enclosed by the multipoint interferometer [43]. In this paper, we verify this statement by measuring the position and vorticity of optical vortices in a speckle pattern.

4.2 Experiment

To demonstrate the use of a multi-pinhole interferometer for measuring optical vortices in a speckle pattern, we built a setup as shown in figure 4.1. We illuminate a light shaping diffuser, a specially designed ground glass plate, by a helium-neon laser to create a speckle pattern. At a sufficiently large distance to guarantee fully developed speckle, a multi-pinhole interferometer is mounted on a translation stage. The stage further holds a lens and a CCD camera to record the far field interference pattern behind the multi-pinhole interferometer. The translation stage can be moved in the x and y-direction. In this paper we only present the results for a scan in one direction since we believe that this gives the clearest demonstration of the principle.

A multi-pinhole interferometer consists of N pinholes uniformly distributed on a circle with radius b. As shown in [27], the interference pattern behind such an interferometer contains information on the vorticity of the illuminating optical field for $N \geq 4$ and the number of vortex modes that can be detected depends on N. For an odd number of pinholes, N different vortex modes can be distinguished, while this reduces to $N/2+1$ modes for an even number of pinholes as one cannot distinguish between positive and negative values of ℓ in this case. In a speckle pattern, one only expects vortices with $\ell = \pm 1$. For the above reasons, a multi-pinhole interferometer with $N = 5$ is used in this experiment, which allows detection of optical vortices with $\ell = 0, \pm 1, \pm 2$.

The distance between the light shaping diffusor an the multi-pinhole interferometer is chosen such that the generated speckle is fully developed and that the average distance between two speckles at the interferometer is $X_{sp} \sim 1$ mm. The radius of the interferometer is $a = 100$ µm, which is much smaller than the average speckle size to reduce the possibility that two vortices impinge the multi-pinhole interferometer at the same time. The diameter of the pinholes is $b = 50$ µm, which is the largest pinhole diameter available to garuantee as much throughput as possible. In this experiment, the translation stage is moved in the x-direction over 3 mm and the interference pattern is recorded after every 50 µm. Around the positions where the interference pattern changes because of the presence of an optical vortex, the distance between two consecutive measurements is reduced to 10 µm to improve the resolution.

Direct measurement of the speckle field intensity in the point under study is not possible in the current setup. Instead we determine the total intensity in the recorded interference patterns which is proportional to the total intensity in a small ring around the point under study. Since the intensity around a singularity varies approximately linearly with the distance from the singularity, a minimum in the total intensity in the image implies a minimum in the field intensity at this point.

4.3 Results

Figure 4.2 shows the interference patterns behind the multi-pinhole interferometer at two different positions in the speckle pattern. By comparing these patterns to the patterns published in [27], one can see that the interference pattern in figure 4.2 (a) corresponds to the pattern for an optical vortex with $\ell = 0$, while figure 4.2 (b) resembles the interference pattern for an optical vortex with $\ell = -1$. The orientation of the patterns is determined by the orientation of the multi-pinhole interferometer with respect to the CCD camera. The Fourier transform analysis as presented by Guo et al. allows a quantitative analysis of these interference patterns [41].

Due to the random nature of the fully developed speckle pattern, the local propagation direction of the light impinging the multi-pinhole interferometer varies, causing the interference pattern to move on the CCD-camera. Before the Fourier transform analysis is applied, the interference pattern is first centred on the image.

Guo et al. showed that the relative phases ψ at the pinholes can be determined from the phase of the Fourier transform of the interference pattern behind a multi-pinhole interferometer. They showed that the relative phases can be extracted from the vertices of a polygon, that is a scaled and shifted copy of the multi-pinhole interferometer. Since we

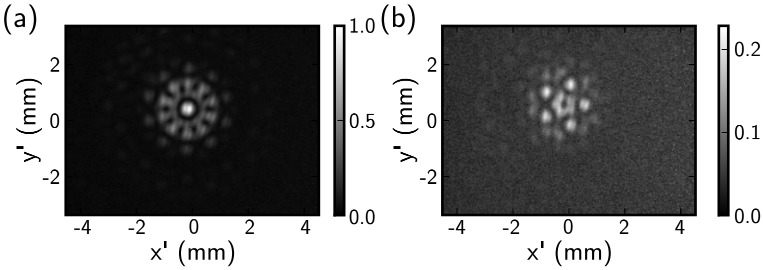

Figure 4.2: Interference patterns behind the multi-pinhole interferometer recorded at two different positions in the speckle pattern. (a) shows the interference pattern at relative position $x = 0\,\mathrm{mm}$, a region of high field intensity. (b) shows the interference pattern at relative position $x = 1\,\mathrm{mm}$, a region of low field intensity. The changing pattern is explained by an optical vortex impinging the multi-pinhole interferometer in (b). The size of each pixel in the CCD image is $6.5\,\mu\mathrm{m}$ and both images contain 1392×1040 pixels. Both images are recorded using the same settings of the CCD-camera and are normalised to the peak intensity of image (a), allowing a direct comparison of the total intensities in the images.

use a multi-pinhole interferometer with five pinholes, the polygon is in fact a pentagon.

Figure 4.3 (a) shows the phase of the Fourier transform of the interference pattern in 4.2 (b). For clarity the aforementioned pentagon is overlaid on the phase of the Fourier transform. Due to the symmetry of the multi-pinhole interferometer, this pentagon can be drawn in ten different orientations (not drawn in figure 4.3 (a)). To reduce the effect of the noise, we determine the relative phases at the pinholes for each of the ten different orientations of the pentagon and average these. Figure 4.3 (b) shows the average relative phases for figure 4.3 (a), where ϕ denotes the azimuthal angle, and gives a comparable result to figure 3 (b) in [41], showing that the optical vortex impinging the multi-pinhole interferometer in this case has topological charge $\ell = -1$. The vorticity of the field impinging the multi-pinhole interferometer is determined by fitting a line through the averaged phase profile and determining the value of the fit at $\phi = 2\pi$.

In total 93 interference patterns were recorded as a function of position in the speckle pattern. Figure 4.4 shows the results of the data analysis for all these patterns. The total intensity in each image is shown in figure 4.4 (a), where the curve is normalised to its maximum and shows two minima. The minimum around $x = 1\,\mathrm{mm}$ corresponds to the image shown in figure 4.2 (b). From figure 4.4 (b) it is clear that this position can be associated with an optical vortex of topological charge $\ell = -1$. The minimum at $x = 2.6\,\mathrm{mm}$ proves to be associated with an optical vortex of topological charge $\ell = 1$ (see Fig. 4.4 (b)). The width of the plateau of both peaks in figure 4.4 is $\sim 100\,\mu\mathrm{m}$, which confirms the fact that an optical vortex can be observed as long as its axis lies well within the multi-pinhole interferometer.

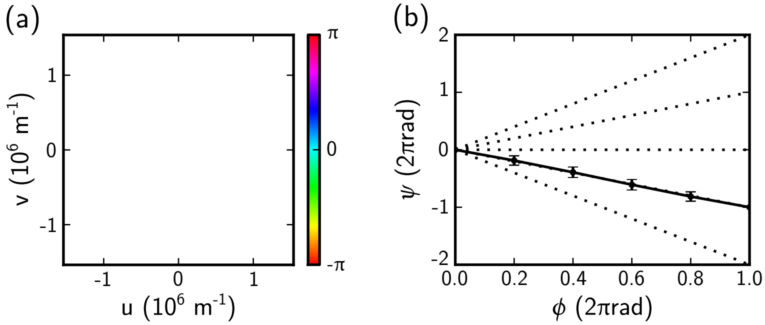

Figure 4.3: (a) Phase of the Fourier transform of the interference pattern in figure 4.2 (b). As a guide to the eye the positions where the relative phase is read off are shown as the vertices of the white pentagon. The same pentagon can be drawn in ten different orientations. (b) shows the average phase at the individual pinholes ψ calculated from the ten different orientations as a function of the azimuthal angle ϕ. The dotted lines are drawn as a guide to the eye and indicate the relative phases for optical vortices of topological charge $\ell = 2, 1, 0, -1, -2$ from top to bottom.

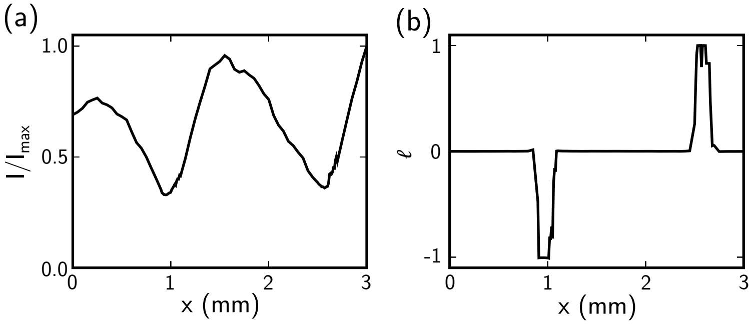

Figure 4.4: (a) Normalised total intensity in the recorded interference patterns as a function of multi-pinhole interferometer position x. Since this intensity is proportional to the intensity in a small ring around the vortices, it is expected not to go to zero. (b) Vorticity of the field impinging the multi-pinhole interferometer as calculated using the Fourier transform analysis. The two minima in (a) clearly correspond to optical vortices of opposite sign.

4.4 Discussion

We demonstrated that a multi-pinhole interferometer is an efficient tool for finding and characterising optical vortices in a speckle pattern. The main advantage of this technique is in the fact that it does not require an additional flat wave front to interfere with the speckle. In addition, this method relies only on a finite number of point measurements and can therefore be scaled to arbitrary sizes, making it applicable to the case where the speckle pattern is much larger than the detector area. The pinholes can be replaced by telescopes and optics to combine the light from them. For electromagnetic fields at lower frequencies wave pipes or electronics can be used to transport and combine the signals.

An important application is foreseen in finding optical vortices in speckled astronomical wave fronts. A more detailed study has to be performed on the exact nature of the speckles that can be expected in astronomical wave fronts.

Some care has to taken in choosing the separation between the pinholes or telescopes. The average speckle size determines both the lower and upper limit of this separation. The pinholes cannot be placed too close to the vortex, since there is hardly any intensity. On the other hand, as the pinholes are placed too far apart, neighbouring vortices start to affect the measurement. We found that a pinhole separation that is roughly one tenth of the average speckle size is a good trade-off.

Combining a large number of multi-pinhole interferometers in a single array would make it possible to find a large number of optical vortices in a wave front in one measurement. Knowledge of the position and vorticity of these vortices makes it possible to reconstruct the wave front, making such an array suited to be used as a wave front sensor. The ability to detect optical vortices is an advantage over existing wave front sensors like the Shack-Hartmann sensor, although a more detailed study has to be carried out to compare the performances of both sensors.

4.5 Conclusion

We demonstrated that a multi-pinhole interferometer, using only a finite number of apertures, can be used to quantitatively map the vorticity in a fully developed speckle pattern. To our understanding this is the first method to measure optical vortices in a speckle pattern without the need for a reference wave front. In addition a multi-pinhole interferometer can, in principal, be scaled to arbitrary sizes, which allows measurement of optical vortices in speckle patterns with any given speckle size.

CHAPTER 5

Quantitative mapping of the optical vortices in a speckle pattern

In previous chapters, we have demonstrated that a multi-pinhole interferometer can be used to measure the topological charge of an optical vortex. We further showed that this method can be used to find the optical vortices in a speckle pattern. Here, we show that a multi-pinhole interferometer can also be used to make a two-dimensional map of an optical field in terms of radially independent optical vortex components, $\exp(im_{\circlearrowleft}\phi)$, where $m_{\circlearrowleft}$ is an integer. From these maps, we can not only determine the position and topological charge of the optical vortices in the field, but also their anisotropy and their orientation. We present results for an isotropic optical vortex and a speckle pattern containing several vortices. The results from the latter case can serve as the starting point to experimentally study the statistics of the anisotropy and orientation of optical vortices in a speckle pattern.

G. C. G. Berkhout, Y. O. van Boheemen, M. P. van Exter, and M. W. Beijersbergen, in preparation for publication.

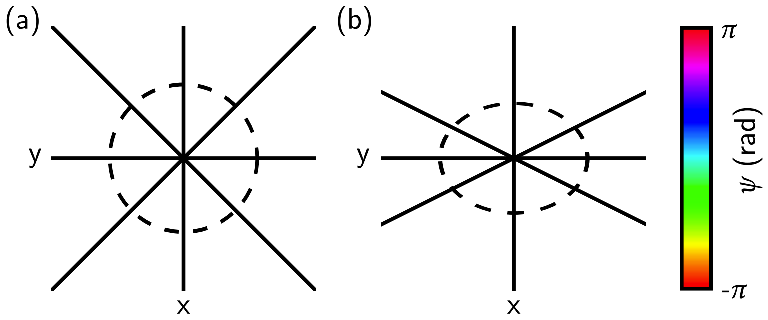

Figure 5.1: Phase of the field for (a) an isotropic $\ell = 1$ optical vortex and (b) an anisotropic $\ell = 1$ optical vortex. The black lines indicate equal phase lines and are spaced $\pi/4$ radians apart. In (b) the lines are more closely spaced around the y axis, showing the anisotropic character of the vortex. In addition, the dashed lines indicate lines of constant intensity. For an isotropic optical vortex, the lines of constant intensity are circles, while for an anisotropic optical vortex they are ellipses.

5.1 Introduction

Optical vortices are of great importance in optics, both for their fundamental properties and their connection to the orbital angular momentum of light [1, 25], as well as for their applications in optical communication [30, 33] and coronography [21].

Optical vortices are associated with phase singularities in an optical field. Isotropic or pure optical vortices are characterised by a complex amplitude whose azimuthal behaviour is characterised by, $A(\phi) \propto \exp(i\ell\phi)$, where ℓ is the topological charge, i.e., the integer number of multiples of 2π that the phase of the field increases in a full turn around the vortex. For an isotropic optical vortex, this phase increase goes linear with the azimuthal coordinate, ϕ. However, in general, this phase increase does not have to be linear, in which case the vortex is called anisotropic (see figure 5.1 for a comparison). Not only does the phase increase in a nonlinear fashion around an anisotropic vortex, also the intensity profile around it is anisotropic, meaning that the lines of constant intensity are ellipses [44], which is indicated by the dashed lines in figure 5.1. Describing the azimuthal behaviour of the field around an anisotropic optical vortex requires more than one pure optical vortex mode, such that the field can be decomposed in the orthogonal basis of pure vortex modes

$$A(\phi) = \sum_{m_\ell} \frac{\lambda_{m_\ell}}{\sqrt{2\pi}} e^{i m_\ell \phi}, \tag{5.1}$$

where the factor $1/\sqrt{2\pi}$ ensures normalization. The coefficient λ_0 is related to the local intensity of the field, while the coefficients λ_{-1} and λ_1 are related to the derivatives of the field. In the case of an isotropic optical vortex, $\lambda_{m_\ell} = \delta_{m_\ell,\ell}$, where $\delta_{i,j}$ is the Kronecker delta.

Anisotropic optical vortices occur in speckle patterns, which arise naturally from the interference of a large number of more or less random plane waves. At particular places in a speckle pattern the amplitude of the field vanishes, causing the phase to be singular. Around these phase singularities an optical vortex is formed, whose exact form is determined by the local interference of the plane waves. Several parametrisations have been proposed to characterise the behaviour of the field around such a vortex. In [9], Freund introduced two parameters to describe the field, which he called the anisotropy and skewness. However, the division between anisotropy and skewness depends on the overall phase of the optical field. This was pointed out by Schechner and Shamir [45], who claimed that the parameters introduced by Freund are inconvenient as ”they are not functionally independent of each other.” The true independent parameters are the anisotropy of the vortex and the orientation of the major semi-axis of the ellipse shown in figure 5.1 (b). A detailed description of these parameters is given in [32, 44, 46]. In [44], the statistical distributions of the anisotropy and orientation in a speckle pattern are given. Experimental verification of the distribution of the anisotropy has been shown in [38].

A convenient way to find the optical vortices is to interfere the speckle pattern with a reference beam [8, 38, 47], which allows reconstruction of the phase around the phase singularity. From this phase reconstruction, the topological charge, anisotropy and orientation of the optical vortex can be determined.

In previous chapters we have described a different method to measure the topological charge of an optical vortex using a multi-pinhole interferometer (MPI). In chapter 4, we have shown that this method also works for finding optical vortices in a speckle pattern. Here, we demonstrate that we can use an MPI to map a field in terms of its pure optical vortex components, in other words, that we can find the coefficients λ_m for each position in the field. From these coefficients, we can determine the position of the optical vortices and their topological charges as well as their anisotropy and orientation.

We present results for an isotropic optical vortex with $\ell = -1$ and a speckle pattern. The latter case can serve as a starting point for studying the statistics of the anisotropy and orientation of the optical vortices in a speckle pattern.

5.2 Theory

A general MPI consists of N pinholes with diameter b, positioned equidistantly on the circumference of a circle with radius a. Provided that the pinholes do not overlap, the transmission function of the MPI, $T(x,y)$, is given by

$$T(x,y) = \sum_{k=0}^{N-1} \mathrm{circ}(x - x_k, y - y_k), \tag{5.2}$$

where

$$\mathrm{circ}(x,y)=\begin{cases}1 & \text{if } \sqrt{x^2+y^2}\le b/2\\ 0 & \text{if } \sqrt{x^2+y^2}>b/2\end{cases}, \tag{5.3}$$

and $(x_k,y_k)=(a\cos\alpha_k, a\sin\alpha_k)$ is the centre of the k-th pinhole with $\alpha_k=2\pi k/N$. The diffraction pattern behind the MPI is given by

$$I(u,v)\propto\left|\mathcal{F}\{A(x,y)T(x,y)\}\right|^2, \tag{5.4}$$

where $A(x,y)$ is the complex field incident on the MPI, and $\mathcal{F}$ denotes the Fourier transform. If the pinholes are small compared to the scale of the fluctuations in the incident field, the amplitude and phase of this field can be considered to be constant over the area of a pinhole, and the diffraction pattern can be written as (see [27, 41])

$$I(u,v)\propto\left|\sum_{k=0}^{N-1}A_k\mathcal{F}\{\mathrm{circ}(x-x_k,y-y_k)\}\right|^2, \tag{5.5}$$

where $A_k=|A_k|\exp(i\phi_k)$ is the complex amplitude of the field incident on the k-th pinhole and $|A_k|$ and ϕ_k are the amplitude and phase respectively. If the MPI is illuminated with an optical vortex, the observed diffraction patterns depend in a qualitative way on the topological charge of the vortex [27]. A more quantitative analysis of the diffraction patterns is presented in [41]; this analysis is based on taking the numerical Fourier transform of the diffraction patterns, which is given by

$$\begin{aligned} g(x,y) &\propto \mathcal{F}^{-1}\{I(u,v)\} &(5.6)\\ &\propto \sum_{k,l=1}^{N-1}P_{kl}A_kA_l^*, &(5.7)\end{aligned}$$

where * denotes the complex conjugate and

$$P_{kl}(x,y)=\int \mathrm{circ}(\alpha-x_k,\beta-y_k)\mathrm{circ}(\alpha-x_l-x,\beta-y_l-y)d\alpha d\beta, \tag{5.8}$$

and the integral is taken over the entire area of the image. Although the input of the Fourier transform is a real-valued intensity image, $I(u,v)$, its output $g(x,y)$ is complex valued. Moreover, $g(x,y)$ is the convolution of the complex field just after the MPI with its complex conjugate. In the special case that the MPI consists of an odd number of pinholes and the diameter of the pinholes is not more than half the separation between them, $g(x,y)$ consists of a number of discrete peaks that are located at (x_k-x_l,y_k-y_l) and given by

$$g(x_k-x_l,y_k-y_l)\propto A_kA_l^*, \tag{5.9}$$

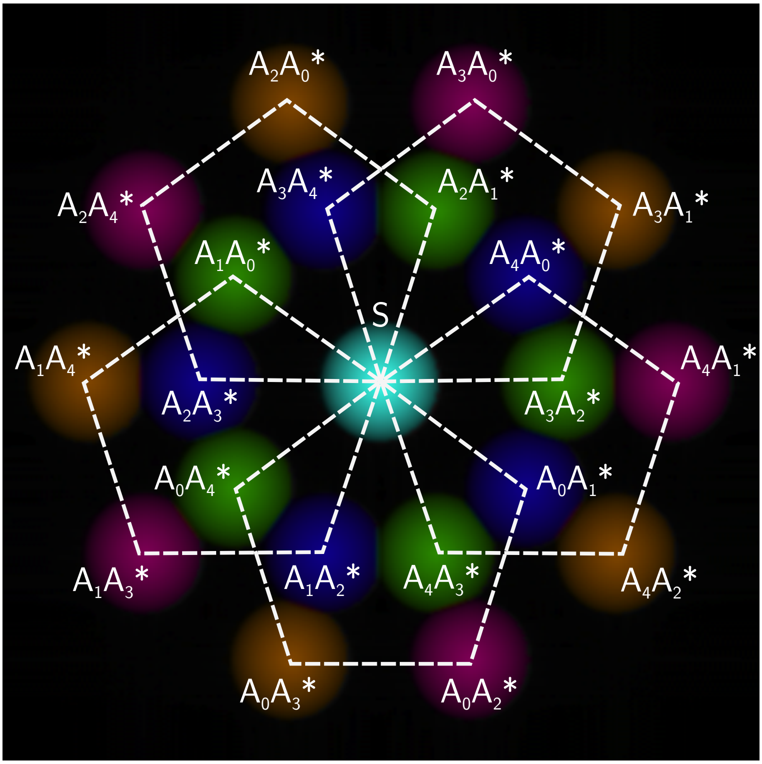

Figure 5.2: Graphical representation of equation 5.9 for an $N = 5$ multi-pinhole interferometer illuminated with an on-axis and centred $\ell = 1$ optical vortex. Each of the 20 spots corresponds to a cross-product, $A_k A_l^*$. In addition, the central peak is given by $S = \sum_{k=0}^{N-1} |A_k|^2$. As a guide to the eye, $N = 5$ dashed pentagons are drawn, which will be used in the analysis described in section 5.3.

where A_k and A_l are the complex amplitudes at the k-th and l-th pinhole, respectively. Interestingly, each peak corresponds to a single product of the amplitudes at two pinholes. Figure 5.2 shows a typical example of equation 5.6 for $N = 5$. Because the input signal of the Fourier transform, $I(u, v)$, is real valued, $g^*(x, y) = g(-x, -y)$ which can be clearly seen in the figure.

From the set of cross-products, $A_k A_l^*$, the amplitude of the field at each of the pinholes can be determined (details of this analysis are provided in section 5.3). Once the complex amplitudes are determined, these can be rewritten in the basis of radially independent optical vortex modes

$$A_k = \sum_{m=-(N-1)/2}^{(N-1)/2} \frac{\lambda_m}{\sqrt{2\pi}} e^{im(2\pi k/N)}. \tag{5.10}$$

As explained in chapter 2, an MPI with and odd number of pinholes N can only detect N

different vortex modes and hence the summation in equation 5.10 runs from $m_\ell = -\frac{N-1}{2}$ to $m_\ell = \frac{N-1}{2}$. We further define $\gamma_{m_\ell} \equiv |\lambda_{m_\ell}|^2$.

Once we have decomposed the field in the aforementioned basis, we can use the results to calculate the anisotropy and orientation of the optical vortex using the equations given in [44]

$$s_3 = \frac{\gamma_1 - \gamma_{-1}}{\gamma_1 + \gamma_{-1}}. \tag{5.11}$$

Finally, we can calculate the orientation of the optical vortex by

$$\phi_0 = \frac{1}{2}(\arg \lambda_1 - \arg \lambda_{-1}). \tag{5.12}$$

5.3 Analysis

To extract the complex amplitudes at the pinholes from the diffraction patterns behind an MPI, we apply the following analysis steps:

1. Centre the diffraction patterns on the CCD-image and crop the image;
2. Calculate the inverse discrete Fourier transform (IDFT);
3. Determine the complex peak amplitudes of all $N(N-1)+1$ peaks in the IDFT image;
4. Derive the complex amplitudes, A_k, at the pinholes;
5. Rewrite these amplitudes in terms of the radially independent vortex modes (coefficients λ_k);
6. Calculate the anisotropy and orientation of the optical vortex.

Below we describe these steps in more detail.

Due to the fact that the MPI moves, while the CCD-camera is fixed, the diffraction pattern moves across the CCD-camera as the stage moves, which affects the Fourier transform of the image. To avoid this, we first determine the centre of the diffraction patterns by making use of the Bessel function amplitude envelope, caused by the diffraction at the individual pinholes. We do so by convoluting the diffraction pattern with the Bessel pattern expected from a single pinhole and determining the maximal overlap between the two images, which corresponds to the centre of the diffraction pattern. Once the centre of the diffraction pattern is determined, the pattern is shifted such that its centre coincides with the centre of the image, by circularly rotating the pixels in both the x and y direction. The original image has 768×512 pixels. After centring, the image is cropped to 512×512 pixels, by removing 128 columns of pixels on either side of the image.

We take the complex discrete Fourier transform of this centred and cropped image, which returns an image as described by equation 5.9. Due to the fact that we use a discrete

Fourier transform, the position, (x_{kl}, y_{kl}), and diameter, s, of all $N(N-1)+1$ peaks in the Fourier transformed image is scaled and given by

$$
\begin{aligned}
(x_{kl}, y_{kl}) &= \frac{nd}{\lambda z}(x_k - x_l, y_k - y_l), && (5.13)\\
s &= \frac{nd}{\lambda z} b, && (5.14)
\end{aligned}
$$

where a and b are the dimensions of the multi-pinhole interferometer, $z = 0.1$ m is the distance between the MPI and the CCD, $\lambda = 633$ nm is the wavelength, $n = 512$ is the number of pixels, and $d = 9.0$ µm is the pixel size. For convenience, we define $S_{kl} \equiv A_k A_l^*$ and use the positions given in equation 5.13 as a starting point for finding the peak amplitudes $|S_{kl}|$. The absolute value of the complex amplitude around these peaks, $|g(x,y)|$ around these peaks is described by the convolution between two pinholes which is described by

$$|g(x,y)| = c\sqrt{(x-x_{kl})^2 + (y-y_{kl})^2} + |S_{kl}|, \tag{5.15}$$

where c is a negative constant. We fit this function to the amplitude of the transformed image around each of the peak positions (x_{kl}, y_{kl}) and find the peak amplitudes $|S_{kl}|$. The phase can be directly determined from the phase of $g(x,y)$, which can be combined with $|S_{kl}|$ to give the complex value of S_{kl}. In addition, we determine the peak amplitude of the central peak in the Fourier transform, S. To do this, we perform a fitting routine similar to the one described in equation 5.15, but remove the central pixel of the Fourier transform, since this pixel alone contains all the background offset of the original image.

From this set of S_{kl}, we can determine the complex amplitude of the field at the pinholes. For each fixed value of l, we can apply the following analysis. For demonstration purposes, we take $l = 0$ and use

$$A_k A_0^* \equiv S_{k0}, \tag{5.16}$$

for $k = 1 \ldots N-1$. In addition, the intensity of the central peak of the Fourier transformation is given by

$$
\begin{aligned}
S &= \sum_{k=0}^{N-1} |A_k|^2\\
&= |A_0|^2 + \sum_{k=1}^{N-1} \left|\frac{S_{k0}}{A_0}\right|^2, && (5.17)
\end{aligned}
$$

where we used equation 5.16 to get to the second part of this equation. Equation 5.17 can be solved for A_0

$$|A_0| = \sqrt{\frac{1}{2}\left(S - \sqrt{S^2 - 4S_0}\right)}, \tag{5.18}$$

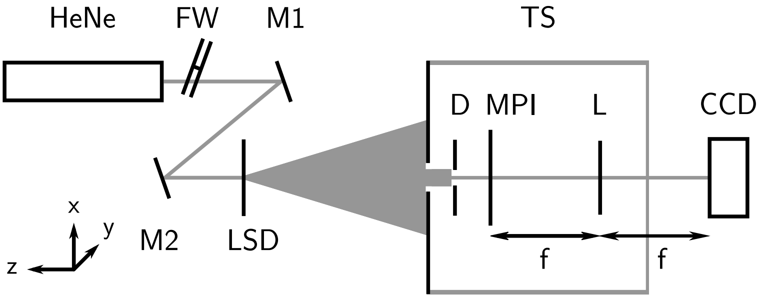

Figure 5.3: Schematic overview of the setup used to measure a map of the pure vortex modes in a complex field, and thereby the position, charge, anisotropy and orientation of the vortices contained in the field. We use the setup to study the far-field of a fully developed speckle pattern, which is generated by illuminating a light shaping diffuser (LSD) with a helium-neon (HeNe) laser beam. The LSD can be replaced by a fork hologram, which produces isotropic optical vortices. Two mirrors (M1 and M2) and a filter wheel (FW) are used to steer and attenuate the beam. The MPI is mounted on a translation stage (TS) that can moved in the x- and y-direction. An iris (D) is used to shield the MPI from any stray light. The far-field diffraction pattern behind the MPI is recorded with a lens (L) and a CCD-camera, which is fixed to the optical table.

where $S_0 = \sum_{k=1}^{N-1} |S_{k0}|^2$. Since we can determine the field up to an overall phase, we choose the phase of A_0 to be 0. From equation 5.16 and the obtained values for S_{k0} we can now determine A_k for $k = 1 \ldots N-1$. This analysis can be repeated for $l = 1 \ldots N-1$, which reduces the noise in the determined amplitudes.

Finally we rewrite the obtained complex amplitudes in the basis of radially independent optical vortex modes using equation 5.10 and calculate the anisotropy and orientation of the vortex using equations 5.11 and 5.12, respectively.

5.4 Experiment

To experimentally measure a map of the pure vortex modes in a complex field, and thereby the position, charge, anisotropy and orientation of the vortices contained in the field, we use the setup shown in figure 5.3. In this particular experiment we use an MPI with $N = 5$, $a = 100$ µm and $b = 50$ µm. The stage is used to scan the MPI through the far-field of a fully developed speckle pattern that is generated by illuminating a light shaping diffuser with a helium-neon laser (see figure 5.3 and its caption for more details). The diffuser can be replaced by a fork hologram which generates isotropic optical vortices. For each position of the translation stage the diffraction pattern is captured using the CCD-camera; the image is analysed directly as described above, to avoid storage of large amounts of data.

5.5 Results

To demonstrate the validity of our method, we first analyse the far-field of a fork hologram, which contains an isotropic optical vortex in each of its diffraction orders, except for the zeroth order. We choose the diffraction order that contains a vortex with $\ell = -1$. This vortex is studied with the setup presented previously, where we scanned the MPI in 20 by 20 steps of 20 µm. The results of the analysis are shown in figure 5.4, were we show $\gamma_{m_\perp} \equiv |\lambda_{m_\perp}|^2$, for $m_\perp = 0, \pm 1, \pm 2$. As expected, only the γ_{-1} shows a contribution in the centre of the beam. At the beams edges, the beam starts resembling a flat wave front and, indeed, the γ_0 components becomes dominant.

From the above results, we can derive the anisotropy and orientation of the optical vortices. For the case of the isotropic $\ell = -1$ vortex, we obtain

$$s_3 = 1.00, \tag{5.19}$$

$$\phi_0 = -0.441\pi, \tag{5.20}$$

which proves that our system gives the expected result.

Subsequently, we study a speckle pattern which is scanned with 200 by 200 steps of 20 µm (see figure 5.5). Following the same method, we can calculate the anisotropy and orientation of the vortices in the speckle patterns. The γ_0 components is proportional to the locally averaged intensity of the field and it indeed resembles the intensity of a speckle pattern. One can see several optical vortices of both charge $\ell = -1$ and $\ell = 1$, which show up as bright spots in the γ_{-1} and γ_1 images, respectively. The results from this analysis serve as a starting point for a statistical analysis of the anisotropy and orientation of optical vortices in a speckle pattern.

5.6 Conclusion

We have demonstrated that an MPI can be used to map a field in terms of its optical vortex components. These maps can not only be used to find the positions and topological charges of the optical vortices in the field, but also to determine their anisotropy and orientation. We have presented results for a field with an isotropic optical vortex, which proves the validity of the analysis. In addition, we have shown the optical vortex maps for a speckle pattern, which contains several optical vortices. By studying a large number of these optical vortices, one can determine the statistics and the anisotropy and orientation of these vortices; this is subject for further study.

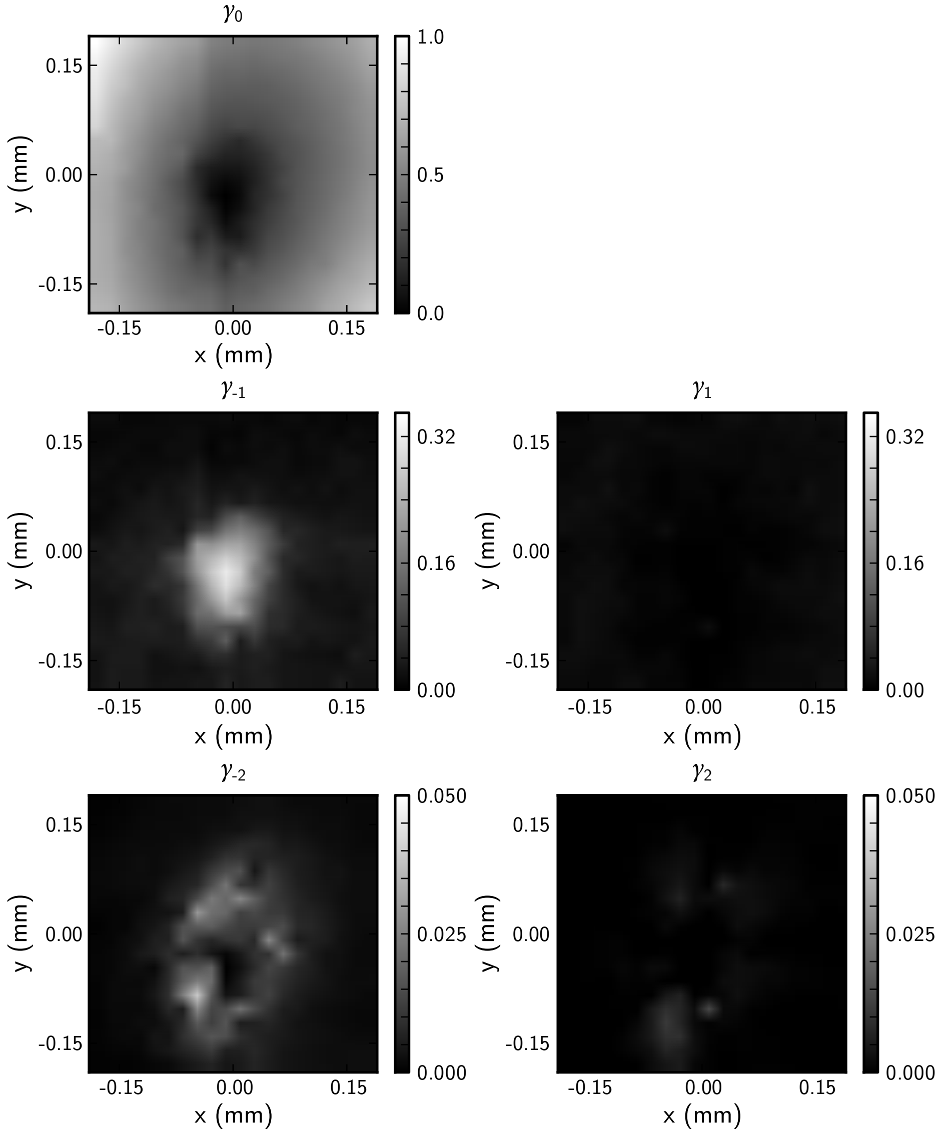

Figure 5.4: Coefficients of the radially independent optical vortex modes in an isotropic $\ell = -1$ optical vortex. As expected only the γ_{-1} is present in and around the centre of the beam. Further away from the centre of the beam, the wave front becomes flatter and γ_0 gives the highest contribution. All images are normalised to the peak of the γ_0 image.

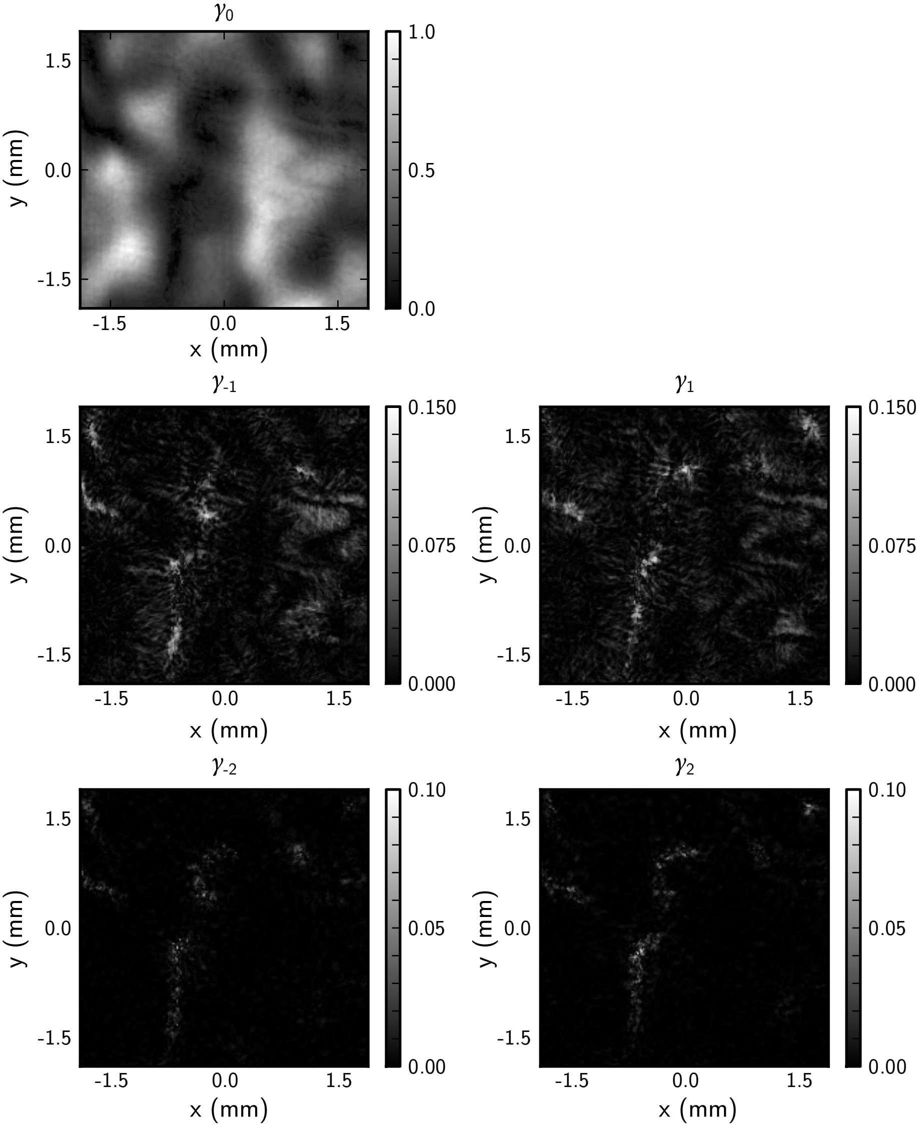

Figure 5.5: Coefficients of the radially independent optical vortex modes in a speckle patterns. The γ_0 is proportional to the locally averaged intensity and indeed resembles an image of a speckle pattern. Several optical vortices, both of topological charge $\ell = -1$ and $\ell = 1$, can be seen as bright spots in the γ_{-1} and γ_1 images, respectively. Detailed study of the area around each vortex will yield the anisotropy and orientation of each of the vortices.

CHAPTER 6

Efficient sorting of orbital angular momentum states of light

We present a method to efficiently sort orbital angular momentum (OAM) states of light using two static optical elements. The optical elements perform a Cartesian to log-polar coordinate transformation, converting the helically phased light beam corresponding to OAM states into a beam with a transverse phase gradient. A subsequent lens then focuses each input OAM state to a different lateral position. We demonstrate the concept experimentally by using two spatial light modulators to create the desired optical elements, applying it to the separation of eleven OAM states.

G. C. G. Berkhout, M. P. J. Lavery, J. Courtial, M. W. Beijersbergen, and M. J. Padgett, *Efficient sorting of orbital angular momentum states of light,* Physical Review Letters **105**, 153601 (2010).

6.1 Introduction

Nearly 20 years ago it was recognized by Allen *et al.* that helically phased light beams, described by a phase cross section of $\exp(i\ell\phi)$, carry an orbital angular momentum (OAM) of $\ell\hbar$ per photon, where ℓ can take any integer value [1, 2, 25]. The unlimited range of ℓ gives an unbounded state space, and hence a large potential information capacity [30, 33]. At the level of single photons, OAM entanglement is a natural consequence of the conservation of angular momentum in nonlinear optics [48]. This entanglement makes OAM a potential variable for increased-bandwidth quantum cryptography [49–51], but only if a single photon can be measured to be in one of many different states.

Generation of helically phased beams with OAM is most usually accomplished using a diffractive optical element, i.e., hologram, the design of which is a diffraction grating containing an ℓ-fold fork-dislocation on the beam axis [52, 53]. If the hologram is illuminated by the output from a laser, or single-mode fiber, the first-order diffracted beam has the required helical phase structure. The same setup, when used in reverse, couples light in one particular OAM state into the fibre. In this case, the hologram acts as a mode specific detector, working even for single photons [29]. However, such a hologram can only test for one state at a time. Testing for a large number of possible states requires a sequence of holograms, thereby negating the potential advantage of the large OAM state space. More sophisticated holograms can test for multiple states, but only with an efficiency approximately equal to the reciprocal of the number of states [33, 54]. For classical light beams, the OAM state can be readily inferred by the interference of the beam with a plane wave and counting the number of spiral fringes in the resulting pattern [15]. One can also use the diffraction pattern behind specific apertures to determine the OAM state of the incoming light beams [27, 55]. All of these approaches again require many photons to be in the same mode so as to produce a well-defined pattern.

The symmetry of helically phased beams means that their rotation about the beam axis induces a frequency shift, each OAM component inducing a separate frequency sideband [56], which could, in principle, be used to measure OAM [30]. However, spinning a beam about its own axis at a rate sufficient to measure its frequency shift is not technically possible. This technical challenge is lessened by using a static beam rotation to introduce an ℓ-dependent phase shift within a Mach-Zehnder interferometer; a cascade of $N-1$ interferometers can measure N different states [13]. Although establishing the principle for single-photon measurement of OAM, for large N, this cascaded interferometric approach remains technically demanding for inclusion into larger systems.

6.2 Theory

In this chapter we are motivated by the simple example of the discrimination of plane waves within direction space. A lens is all that is required to focus a plane wave to a spot in its focal plane, the transverse position depending on the transverse phase gradient of the plane wave. This allows multiple plane waves to be distinguished from each other using a detector array. A requirement for the separation of any two plane waves is an additional phase change of 2π across the aperture of the lens, resulting in a difference in spot positions comparable to the Rayleigh resolution limit. This suggests an approach for separating OAM states, for which a change in mode index of $\Delta\ell = 1$ corresponds to an increment in the azimuthal phase change of 2π. The key optical component in this approach is one that transforms azimuthal position in the input beam into a transverse position in the output beam, i.e., an optical element that transforms a helically phased beam into a transverse phase gradient. This corresponds to the transformation of an input image comprising concentric circles into an output image of parallel lines. Mapping each input circle onto an output line gives the required deviation in ray direction and hence the phase profile of the transforming optical element. However the resulting variation in optical path length means that the transformation introduces a phase distortion that needs to be corrected by a second element. The transforming system therefore comprises two custom optical elements, one to transform the image and a second, positioned in the Fourier plane of the first, to correct for the phase distortion. This transformation is an example of an optical geometric transformation which has been previously studied in the context of optical image processing [57]. It was shown that a geometric transformation can only be implemented by a single optical element if the mapping is conformal. The optical element performs a mapping $(x, y) \mapsto (u, v)$, where (x, y) and (u, v) are the Cartesian coordinate systems in the input and output plane, respectively. In our approach $v = a \arctan(y/x)$ and the conformal mapping requires $u = -a \ln(\sqrt{x^2 + y^2}/b)$, similar to [58, 59]. The phase profile of the transforming optical element is then given by

$$\phi_1(x, y) = \frac{2\pi a}{\lambda f}\left[y \arctan\left(\frac{y}{x}\right) - x \ln\left(\frac{\sqrt{x^2 + y^2}}{b}\right) + x\right], \tag{6.1}$$

where λ is the wavelength of the incoming beam, and f is the focal length of the Fourier-transforming lens. The parameter a scales the transformed image and $a = d/2\pi$, where d is the length of the transformed beam. b translates the transformed image in the u direction and can be chosen independently of a.

The required phase correction can be calculated by the stationary phase approximation [59] and is given by,

$$\phi_2(u, v) = -\frac{2\pi ab}{\lambda f} \exp\left(-\frac{u}{a}\right) \cos\left(\frac{v}{a}\right), \tag{6.2}$$

where u and v are the Cartesian coordinates in the Fourier plane of the first element. Figure 6.1 (a) and (b) show the phase profiles of the transforming and phase-correcting optical element, respectively. One can see that the transforming optical element contains a line discontinuity. The end of this line, i.e., the centre of the phase profile, defines the axis around which the OAM is measured.

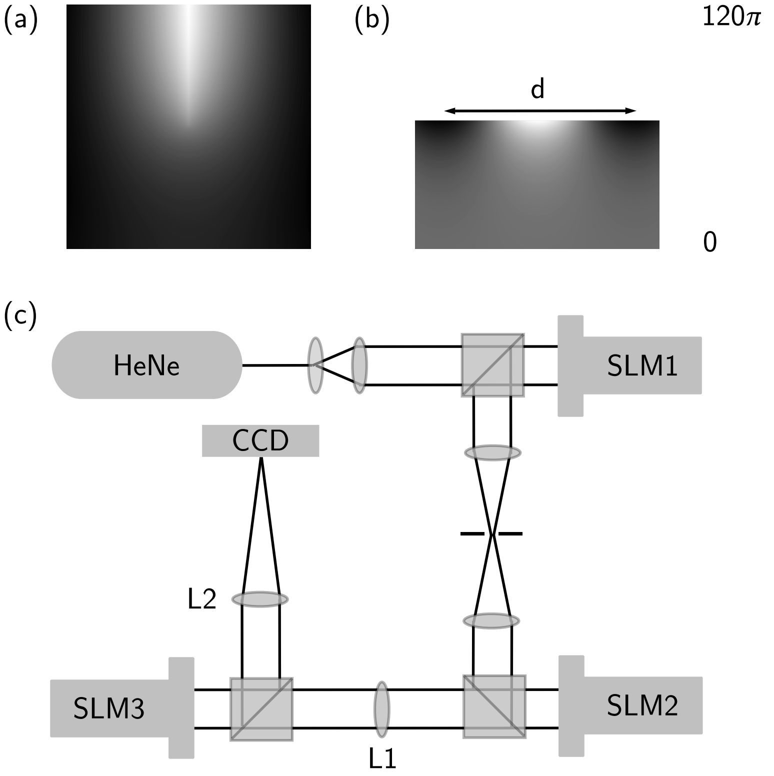

Figure 6.1: Phase profiles of (a) the transforming and (b) the phase-correcting optical element. *d* is the length of the transformed beam. In (b) only that part of the phase-correcting element is shown, that is illuminated by the transformed beam. In the experiment, the phase profiles are displayed on the spatial light modulators (SLMs) with 2π phase modulation. (c) Schematic overview of the setup. We use SLMs to both generate Laguerre-Gaussian beams (SLM1) and create the desired phase profiles for the transforming and phase-correcting optical elements (SLM2 and SLM3, respectively). L1 is the Fourier-transforming lens and L2 focusses the transformed beams. We use beamsplitters to ensure perpendicular incidence on the SLMs.

A lens is inserted after the phase-correcting element to focus the transformed beam, which now has a $2\pi\ell$ phase gradient, to a spot in its focal plane. In the plane of this lens, the transformed beam is rectangular, meaning that the diffraction limited focal spot is elongated in the direction orthogonal to the direction in which the spot moves. The transverse position of the spot changes as a function of ℓ and is given by

$$t_\ell = \frac{\lambda f}{d}\ell. \tag{6.3}$$

6.3 Experiment and results

We use diffractive spatial light modulators (SLMs) to create the desired phase profiles. For monochromatic light, an SLM can be programmed such that any desired phase profile is applied to the first-order diffracted beam, limited in complexity only by the spatial resolution of the SLM. Figure 6.1 (c) shows a schematic overview of the optical system. We use Laguerre-Gaussian (LG) beams as our OAM states. The first SLM, programmed with both phase and intensity information [51], is used to generate any superposition of LG modes. Using relay optics and an iris to select the first-order diffracted beam, this input state is directed onto the transforming element, displayed on the second SLM, which performs the required geometrical transformation in the back focal plane of the Fourier-transforming lens. We choose d such that the transformed beam fills 80% of the width of the phase corrector element in order to avoid diffraction effects at its edges. A third SLM is used to project the phase-correcting element. The diffracted beam from this SLM has a transverse phase gradient dependent on the input OAM state. These direction states are focussed onto a CCD array by a lens and, as discussed above, the lateral position, t_ℓ, of the resulting elongated spots is proportional to the OAM state of the incident beam.

Figure 6.2 shows modeled and observed phase and intensity profiles at various places in the optical system for a range of OAM states. The modeled data is calculated by plane wave decomposition. In the second column, one can see that an input beam with circular intensity profile is unfolded to a rectangular intensity profile with a $2\pi\ell$ phase gradient. As predicted, the position of the elongated spot changes with the OAM input state. We recorded the output of the mode sorter for input states between $\ell = -5$ and $\ell = 5$. The experimentally observed spot positions are in good agreement with the model prediction. Our system further allows us to identify a superposition of OAM states, as can be seen in the final row of figure 6.2, where an equal superposition of $\ell = -1$ and $\ell = 2$ gives two separate spots in the detector plane at the position of $\ell = -1$ and $\ell = 2$. We note that observed spots are slightly broader than the modelled ones, which is due to aberrations introduced by the optical system.

To directly measure the state of any input beam, we define eleven, equally sized, rectangular regions in the detector plane, all centred around one of the expected spot position

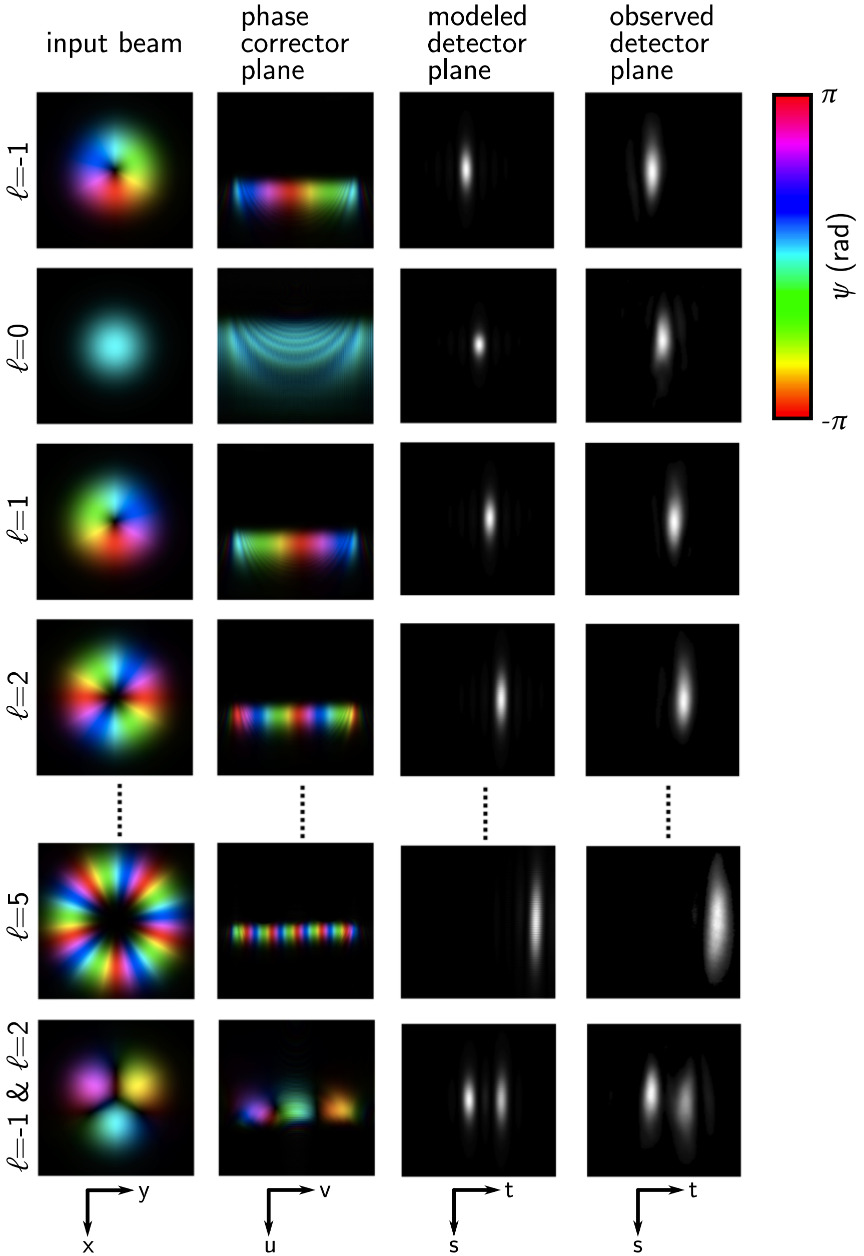

Figure 6.2: Modeled and observed phase and intensity profiles at various planes in the optical system. From left to right, the images show the modeled phase and intensity distribution of the input beam just before the transforming optical element and just after the phase-correcting element, and the modeled and observed images in the CCD plane for five different values of ℓ. The final row shows the results for an equal superposition of $\ell = -1$ and $\ell = 2$. The last two columns are 6× magnified with respect to the first two columns.

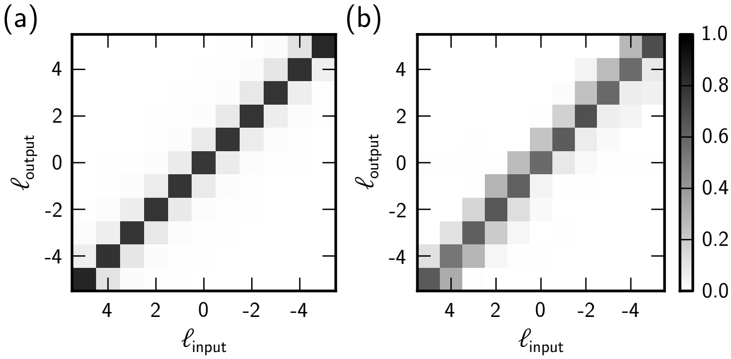

Figure 6.3: Total intensities in all detector regions for pure input OAM states from $\ell = -5$ to $\ell = 5$, for both the (a) modeled and (b) observed results. The regions all have the same size and are chosen such that they fill the entire aperture. The intensities are shown as a fraction of the total intensity in the input beam.

for the eleven input modes used in the experiment. By measuring the total intensity in each of these regions, we can determine the relative fraction of a specific OAM state in the input beam. Figure 6.3 (a) and (b) show the results for eleven pure input states, both modeled and observed, as shown in the third and fourth column of figure 6.2, respectively. Since the spots for two neighboring states slightly overlap, some of the light in a state leaks into neighboring regions, i.e., there is some cross talk between different states. This cross talk shows up as the off-diagonal elements in figure 6.3. As described before, our experimental results show slightly broader spots than the modelled data and hence the off-diagonal elements are slightly larger. It is clearly possible to determine the input state of the light beam from the position of the output spot in the detector plane.

A commonly used measure to quantify the amount of cross talk between channels is the channel capacity, which is the maximum amount of information that can be reliably transmitted by an information carrier [60]. In an optical system, this channel capacity can be quoted as "bits per photon". If a photon can be in one of N input states and its state can be measured perfectly at the output, the channel capacity takes the theoretical maximum value of $\log_2 N$.

Table 6.1 presents the channel capacity of the system for the modeled and observed results, calculated from the data shown in figure 6.3. A generic approach to minimize cross talk is to increase the separation between channels. We therefore consider the cases where we use only every other state, $\Delta\ell = 2$, and every third state, $\Delta\ell = 3$. This approach gives fewer states, but less overlap between different spots. In all cases, due to the experimental imperfections, the channel capacity for the observed data is slightly lower than the modeled one, but for $\Delta l = 3$ it approaches the model very closely.

ℓ	N	$\log_2 N$	Modeled	Observed
1	11	3.46	2.36	1.96
2	6	2.59	2.10	1.93
3	4	2.00	1.70	1.68

Table 6.1: Channel capacity calculated from the results shown in figure 6.3. The first three columns show the separation between the channels, Δl, the number of states taken into account, N, and the theoretical maximum value, $\log_2 N$. The last two columns correspond to the data shown in figures 6.3 (a) and (b), respectively.

6.4 Discussion

We note that the optical transformation is only perfect for rays which are normally incident on the transforming element. Helically phased beams are inherently not of this type, the skew angle of the rays being ℓ/kr [61]. Although this skew angle is small when compared to the angles introduced by the transforming element, it might introduce a slight transformation error which increases with ℓ. If the input is a ringlike intensity profile, the skew angle leads to a sinusoidal distortion from the expected rectangular output. This potential skew ray distortion is reduced by decreasing the propagation distance over which the transformation occurs, i.e., reducing f.

In its present form, our approach is limited by the fact that the resulting spots are slightly overlapping. This is because our transformation discards the periodic nature of the angular variable, using instead only a single angular cycle and producing an inclined plane wave of finite width, and similarly a finite width of spot. One option for improvement is to modify the transformation to give multiple transverse cycles, which results in larger phase gradient and thus a larger separation between the spots, albeit at the expense of increased optical complexity. One approach to implementing this improvement would be to add a binary phase grating to the transforming elements, producing both positive and negative diffraction orders. By adjusting the pitch of the grating appropriately, two identical, adjoining copies of the reformatted image are created in the plane of the phase corrector.

We further recognise that there is a 70% light loss associated with the two SLMs that comprise the mode sorter. This loss could, however, be eliminated by replacing the SLMs with the equivalent custom-made refractive optical elements.

6.5 Conclusion

In conclusion, we have described a novel system comprising of two bespoke optical elements that can be used to efficiently measure the OAM state of light. We have shown numerical and observed data to support our method. The method has a limitation due to the overlap of the spots for different states that could be reduced by applying an additional diffraction grating to the first surface. The system opens the way to many interesting investigations ranging from experiments in multiport quantum entanglement [49], to applications in astrophysics [11] and microscopy [62], all of which make use of the OAM state basis.

CHAPTER 7

Measuring orbital angular momentum superpositions of light by mode transformation

In chapter 6 we reported on a method for measuring orbital angular momentum (OAM) states of light based on the transformation of helically phased beams to tilted plane waves. Here we consider the performance of such a system for superpositions of OAM states by measuring the modal content of noninteger OAM states and beams produced by a Heaviside phase plate.

G. C. G. Berkhout, M. P. J. Lavery, M. J. Padgett, and M. W. Beijersbergen, *Measuring orbital angular momentum superpositions of light by mode transformation,* Optics Letters **36**, 1863 (2011).

7.1 Introduction

Ever since it was first described that a light beam containing an optical vortex, $\exp(im\phi)$, carries an orbital angular momentum (OAM) of $m\hbar$ per photon for integer m [1], this subject has drawn significant interest [25]. In addition to its fundamental properties, the application of OAM in optical communication [33] has been studied.

Optical vortices occur in higher-order laser modes; can be created by means of a mode converter [63], spiral phase plate [5] or fork hologram [52]; and can also be made by encoding the appropriate hologram on a spatial light modulator (SLM) [47]. In addition, optical vortices occur in caustics [64] and speckle patterns [8].

Although creating optical vortices is relatively straightforward, measuring their topological charge, m, is not. Several methods are being used, ranging from interference [15], diffraction [27, 55], holograms [54], q-plates [65] and interferometers [13] to mode specific detection [29]. All these methods have significant disadvantages; they either work only for many photons in the same state, have low throughput, are technically very challenging or can detect only one state at a time.

Recently we have described a system comprising two custom, static optical components that allows simultaneous detection of many different OAM modes (chapter 6). The system is based on performing a Cartesian to log-polar optical transformation [58] that transforms the helically phased beam around an optical vortex into a tilted plane wave. Optical vortices with different topological charges are transformed into plane waves with a different tilt that, in turn, are focused to different positions in the focal plane of a lens. The topological charge is thus encoded in the lateral position of the spot; all radial information is encoded in the orthogonal axis in the focal plane. Because of the design of the optical transformation, the spots will slightly overlap, which limits the use of the system for single photon applications. This could be resolved by changing the design of the two custom components, at the expense of making the optical design more complex [66].

The main advantage of the mode-transforming system is its ability to detect multiple modes at the same time. A spectrum of optical vortices can be generated by spontaneous parametric downconversion [67] or by phase plates, such as noninteger spiral phase plates [68] and angular sector phase plates [69]. A misaligned beam also gives rise to a spectrum of OAM states [70]. Finally, one can create arbitrary superpositions of orbital angular momentum states by displaying the correct superposition of spiral phase plates as a hologram on the SLM.

The modal content of any superposition can be directly derived from the positions and relative intensities of the spots on a detector in the focal plane of the mode sorter. For potential single-photon applications, the position where the photon hits the detector is statistically determined by the input superposition.

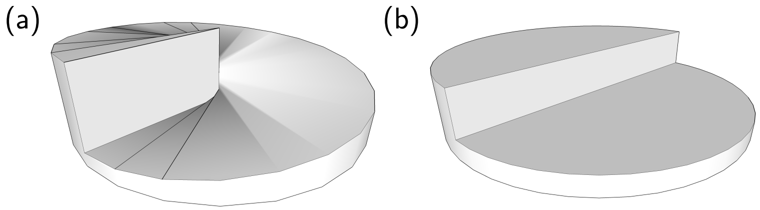

Figure 7.1: Schematic drawing of (a) a spiral phase plate and (b) a Heaviside phase plate.

7.2 Theory

In this chapter, we measure the modal content of noninteger OAM states and beams produced by a Heaviside phase plate (see figure 7.1). Following [69], we can calculate these modal contents theoretically, neglecting the radial dependence. A general superposition of optical vortex states is given by

$$A(\phi) = \sum_{m} \lambda_m A_m(\phi), \tag{7.1}$$

where $A_m(\phi) = \frac{1}{\sqrt{2\pi}} e^{im\phi}$ are the normalized vortex states. The modal coefficients for an arbitrary superposition can be found by

$$\lambda_m = \frac{1}{\sqrt{2\pi}} \int_0^{2\pi} e^{-im\phi} A(\phi) d\phi. \tag{7.2}$$

We further define $\gamma_m = |\lambda_m|^2$. The normalization of the vortex states guarantees that $\sum_m \gamma_m = 1$.

A noninteger OAM state is given by $\exp(iQ\phi)$, where Q is the non-integer topological charge. From equation 7.2, we calculate that

$$\lambda_m = \mathrm{sinc}((Q - m)\pi) e^{i(Q-m)\pi}, \tag{7.3}$$

which reduces to $\lambda_m = \delta_{m,Q}$ if Q becomes integer, where $\delta_{i,j}$ is the Kronecker delta.

In addition to the noninteger spiral phase plate, we measure the modal content of the field behind a Heaviside phase plate, which is characterised by a phase step of π between the two halfs of the phase plate, resulting in a spectrum as defined in [69].

7.3 Experiment

A schematic overview of the experimental setup is shown in figure 7.2. Although it is possible to manufacture all required optical components from glass or plastic, we encode them on three SLMs, which can be used to imprint any spatially varying phase to a beam.

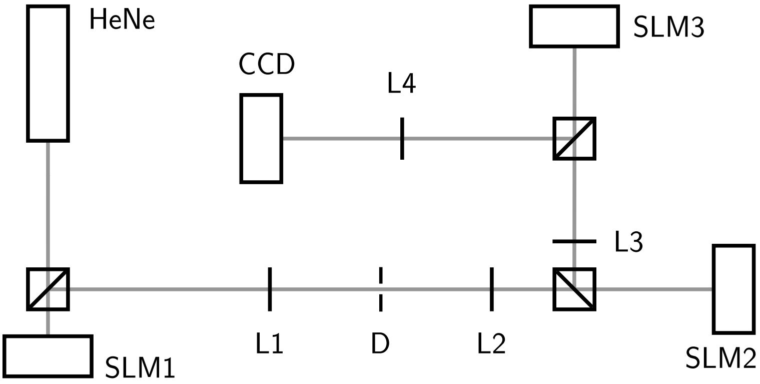

Figure 7.2: Schematic overview of the setup. See text for details.

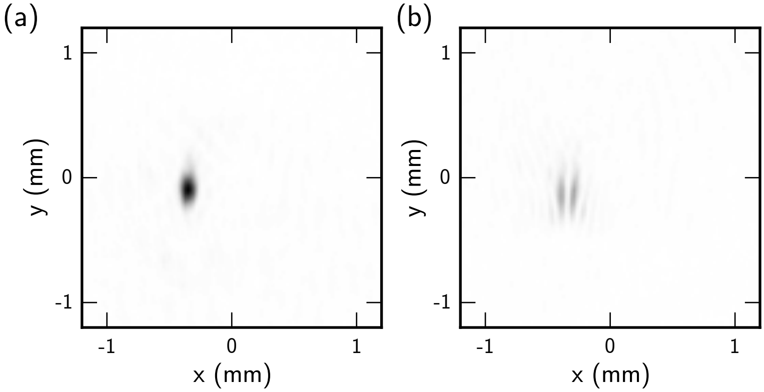

Figure 7.3: CCD images for an equal superposition of two modes ($\ell = -1$ and $\ell = 0$) with a relative phase of (a) $\psi_i = 0$ and (b) $\psi_i = \pi$. Both images are scaled to the peak intensity of the image shown in (a). The color scale is inverted for clarity.

SLM1 is used to create all input states, either by encoding a noninteger or Heaviside phase plate or by encoding an arbitrary superposition of spiral phase plates. The input states are imaged onto SLM2 using two lenses (L1 and L2) and a diaphragm (D) to filter out the correct diffraction order. The mode sorter, whose phase profiles are described in chapter 6, comprises two SLMs (SLM2 and SLM3), together with a lens (L3). A lens (L4) is used to focus the output of the mode sorter onto a CCD camera. We use beam splitters to ensure perpendicular incidence on all SLMs.

7.4 Results

As described above, the position of the focussed spot on the CCD camera depends on the OAM state of the input beam. For a superposition, we expect to see more than

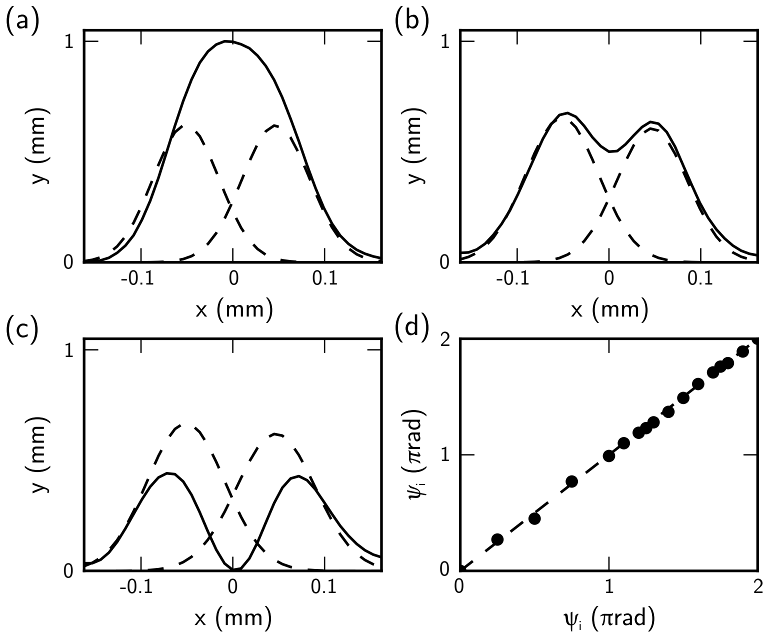

Figure 7.4: Summed CCD images with a relative phase of (a) $\psi_i = 0$ (corresponding to figure 7.3 (a)), (b) $\psi_i = \pi/2$ and (c) $\psi_i = \pi/2$ (corresponding to figure 7.3 (b)) (solid lines). The dashed lines show the fitted peaks of the individual modes. (d) The measured relative phase, ψ_{m_ℓ}, as returned by the fit versus the input relative phase, ψ_i, as set on SLM1.

one spot with relative intensities, depending on the modal content (see figure 7.3 for typical examples). Since there is no extra information in the y axis of the CCD images, we sum them over the rows to increase the signal-to-noise ratio. We extract the relative amplitudes from these summed images by fitting a sum of the theoretically expected peaks for the individual modes. In the fitting routine, we allow some margin in the peak position and the peak width to compensate for possible experimental errors.

We study the output of the mode sorter for an equal superposition of two modes ($m_\ell = -1$ and $m_\ell = 0$) with changing relative phase. Figure 7.4 (a-c) show typical summed images. Note that one can only see the effect of the relative phase in the regions where the peaks overlap and interfere constructively or destructively, depending on the relative phase. In addition, figure 7.4 shows the fitted peaks of both modes as dashed curves. The fit returns the amplitudes of the peaks and the relative phase between the states. Figure 7.4 (d) shows the fitted relative phases for a number of input phases, as set on SLM1. This figure demonstrates that the relative phase between the states in conserved by the transformation. The output relative phases also depend on the angular orientation of the mode sorter around the optical axis. All data are corrected for this orientation.

Figure 7.5 (a-e) shows the modal decomposition for noninteger OAM states, both theoretical as calculated from equation 7.3 (black), and exprimental (gray), where $\mathcal{Q}$ is varied between $\mathcal{Q} = -1$ and $\mathcal{Q} = 0$. One can clearly see that the peak shifts from $m = -1$ to $m = 0$. For noninteger values of $\mathcal{Q}$, the spectrum broadens. Figure 7.5 (f) shows the results for a Heaviside phase plate. The results of the fits are qualitatively in good agreement with the theoretically predicted values.

7.5 Discussion

We have shown that mode transformation preserves the relative phase between input states and that this relative phase can be measured in regions where the peaks of two transformed modes overlap, which experimentally works fine if the modes have $\Delta m = 1$. An alternative way to measure the relative phase would be interfering the output of the mode sorter with a flat wave front, increasing the complexity of the system. The fact that the mode transformation separates the modes spatially and preserves coherence, could be used to manipulate modes in a superposition.

An important application of a optical vortex mode sorter is in optical communication. The optical vortex states span a higher-dimensional basis, which could be used to encode information in. As shown in this chapter, our mode sorter could be used to decode the information that is in superpositions of neighboring optical vortex states.

7.6 Conclusion

In conclusion, we have shown the principle that our previously presented mode sorter can be used to determine the modal content of OAM superpositions in a single, practical measurement. This system can be used as a decoder in higher-dimensional optical communication schemes based on OAM states.

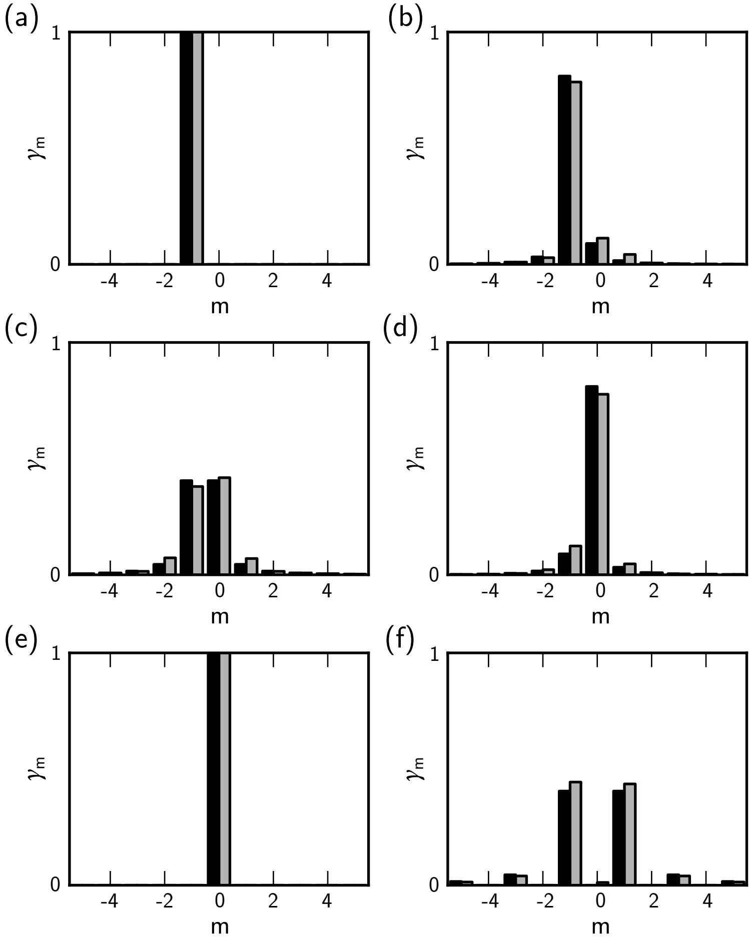

Figure 7.5: Modal decomposition of a non-integer OAM state with (a) $\mathcal{Q} = -1$, (b) $\mathcal{Q} = -\frac{3}{4}$, (c) $\mathcal{Q} = -\frac{1}{2}$, (d) $\mathcal{Q} = -\frac{1}{4}$, (e) $\mathcal{Q} = 0$ and (f) the beam produced by a Heaviside phase plate. Theoretical data is shown in black, experimental data in grey.

CHAPTER 8

Towards applications based on measuring the orbital angular momentum of light

Efficient measurement of the orbital angular momentum (OAM) of light has been a long-standing problem in both classical and quantum optics. In this thesis, we have presented two ways to solve this problem, thus opening the way for applications based on the OAM of light. In previous chapters, we have identified large bandwidth optical communication and the detection of OAM in astrophysics as potential applications. The application of OAM generation and detection will, in general, involve more complex types of light than the monochromatic, coherent laser light that we used to test our detection methods. In this final chapter, we take the first steps towards the development of such applications by addressing two important aspects of detecting OAM in real applications. First we study the response of both detection systems to polychromatic and (partially) incoherent light. Secondly, we study the orthogonality of the output states in one of our detection systems, the mode sorter, and its response to single photons, which are both relevant for applications in large bandwidth optical communication. These first assessments reveal important properties of the OAM detection systems, that, amongst many other aspects, have to be studied in more detail in the development of applications.

8.1 Introduction

Ever since it was found in 1992 that light can carry orbital angular momentum [1], many efforts have been made to measure this quantity, both for beams of light as well as for single photons. A number of different measurement schemes has been described in the literature. It was, for instance, already known before 1992, that one can find wave front dislocations, or optical vortices, in a speckle pattern by interfering the pattern with a flat wave front, such that the optical vortices show up as a characteristic fork-like interference pattern [8]. The OAM of a Laguerre-Gaussian beam is directly linked to the topological charge of the optical vortex at its centre and the interference method can therefore be used to measure this OAM [53]. It does, however, require many photons to be in the same OAM state to build up the interference pattern. Another way to measure the OAM of a light beam is to use special apertures like the multi-pinhole interferometer (MPI) [27] or a triangular aperture [55], that create qualitatively different diffraction patterns for light in different OAM states. Again this requires many photons to be in the same state. One can also use specific holograms to sort orbital angular momentum states spatially [33, 54], but only with an efficiency that is approximately equal to $1/N$, where N is the number of detected states and one again needs many photons to be in the same state.

There are also methods to measure the OAM of a single photon. One of these methods is to test if a single photon is in a specific state or not, by means of a hologram and a single mode fibre [29]. By repeating this test with a series of different holograms, one can build up a statistical average of the OAM states of the input photons. For a single photon, this measurement discriminates between two states and does not benefit from the infinite nature of the OAM state space. The first measurement to discriminate between more than two OAM states for a single photon was described by Leach et al. [13], who used a Mach-Zehnder interferometer combined with a Dove prism to spatially sort photons based on their OAM. The experiment showed the sorting of four OAM states. In order to sort more states, interferometers have to be added to the setup. To sort N different states, one needs $N-1$ Mach-Zehnder interferometers, which is experimentally very challenging. In chapters 6 and 7 of this thesis, we have presented a different scheme to sort OAM states, that is much easier to set up since it consists of only two custom optical elements and two lenses. This mode sorter converts N different input OAM states into N spatially separated output spots, where N is limited only by the accuracy of the optics. The only disadvantage of this system is that the output spots slightly overlap, which limits the accuracy by which one can determine the OAM of a single photon. This can, however, be overcome by modifying the design of the two custom optical elements, an example of which has been given in chapter 6.

The MPI and the mode sorter presented in this thesis have made measuring the OAM of a light beam experimentally much more feasible; in the case of the mode sorter it even works for single photons. This opens the way towards applications of the OAM of light. So far, we have only treated the case of coherent, monochromatic light. Several times however, we have hinted at the possiblity of detecting OAM in light from astrophysical sources and the possibility of astrophysical sources generating light with orbital angular momentum has been treated elsewhere [11, 26, 71]. Light from astrophysical sources will, in general, not be monochromatic and coherent. It is therefore crucial to study the response of both the MPI and the mode sorter to polychromatic and (partially) incoherent light. The idea that partially coherent light can carry OAM has been described extensively in literature [72–76]. It has also been shown that a special class of partially incoherent light beams can, perhaps surprisingly, still produce diffraction patterns with true intensity zeros behind a MPI [18, 42].

A second application of the OAM of light mentioned in this thesis, is its use for high dimensional communication schemes, which has been discussed in the literature [30, 33]. Our mode sorter can form a key part of this application, provided the different OAM states can be separated sufficiently well. In this chapter, we study the channel separation and the response of the mode sorter for single photons.

This chapter provides calculations for relatively simple examples of polychromatic and (partially) incoherent light and is organised as follows. We treat the MPI and the mode sorter in section 8.2 and section 8.3, respectively. In the latter section, we also study the channel separation of the mode sorter and its response in the quantum regime, with concluding remarks in section 8.4.

8.2 Multi-pinhole interferometer

8.2.1 Response to polychromatic light

All results presented in previous chapters were obtained with a helium-neon laser, that has a wavelength $\lambda = 632.816$ nm. Due to thermal expansion of the laser cavity this frequency can vary by only $\Delta\lambda = \pm 0.001$ nm, being limited by the small spectral width of the optical gain. This has a very minute effect on the diffraction pattern behind a multi-point interferometer (MPI), as can be easily seen by considering an $N = 2$ MPI, which is Young's double slit experiment with the slits replaced by pinholes. The far-field diffraction pattern behind the $N = 2$ MPI is given by bright bands on a dark background separated by a distance Δx, which is given by

$$\Delta x = \frac{\lambda z}{2a}, \tag{8.1}$$

where z is the distance from the MPI to the detector and a is the distance from the pinholes to the centre of the MPI. It should be noted that the diffraction pattern scales with λz.

The diffraction patterns behind a general MPI have been extensively discussed in chapter 2 and 3. For $N \geq 4$, they contain information on the topological charge of an impinging optical vortex. These diffraction patterns can be analysed qualitatively by looking at their numerical Fourier transform [41]. This Fourier transformed image shows $2N$

copies of the MPI, that are scaled with respect to the original. For odd N, one can directly determine the relative phase of the incident optical field at each pinhole by determining the phase of the Fourier transformed image at the vertices of one of these copies of the MPI. In addition we can also derive the relative amplitudes of the fields at the individual pinholes, as shown in chapter 5. The radius of the MPI in the Fourier transform, r, and the size of the pinholes, s, are given by

$$r = \frac{n_x d a}{\lambda z}, \tag{8.2}$$

$$s = \frac{n_x d b}{\lambda z}, \tag{8.3}$$

where n_x is the number of pixels in the original image, d the pixel size, a and b the separation and the diameter of the pinholes in the MPI respectively, λ the wavelength and z the propagation distance. In [41], Guo *et al.* state that the phase of the field can be unambiguously determined if the separation between the pinholes is at least two times their diameter. This can be easily understood from the above equation, since for smaller separations the pinholes will overlap in the Fourier transformed image and the phase cannot be unambiguously determined.

As can be seen from equation 8.2, the positions and sizes of the pinholes in the Fourier transformed image not only depend on the separation and diameter of the pinholes in the MPI, but also on the wavelength. If the field impinging on the MPI contains light of multiple wavelengths, the Fourier transformed image will be the addition of images of the pinholes for different wavelengths.

In order to demonstrate this point, we simulated the diffraction pattern behind an MPI for several different input fields. The patterns are shown in figure 8.1 and were recorded behind the same $N = 5$ MPI with $a = 200\,\mu\text{m}$, $b = 50\,\mu\text{m}$, recorded at $z = 0.1$ m. We have simulated the diffraction pattern for three different wavelengths, $\lambda = 633\,\text{nm}$, $\lambda = 700\,\text{nm}$ and $\lambda = 780\,\text{nm}$, and superpositions thereof. To be able to more clearly distinguish the individual modes in the superpositions, we gave the modes a different topological charge. Although this is somewhat artificial, it simulates a superposition of wavelengths and modes and therefore helps to illustrate our point more clearly.

As in previous chapters, we analyse the diffraction patterns by calculating the numerical Fourier transform of the diffraction patterns. Figure 8.2 shows the absolute value of this Fourier transform for the diffraction patterns shown in figure 8.1. As explained before, one can see 10 pentagons in the Fourier transform, where some of the points are shared between two pentagons. The size of these pentagons decreases when the wavelength increases (compare figure 8.2 (a) and (b)). As expected, a superpositions of the patterns for two wavelengths results in the superposition of the two Fourier transformed images. In figure 8.2 (c) these two patterns can still be distinguished, but in figure 8.2 (d), where the wavelengths are closer together, the points start overlapping.

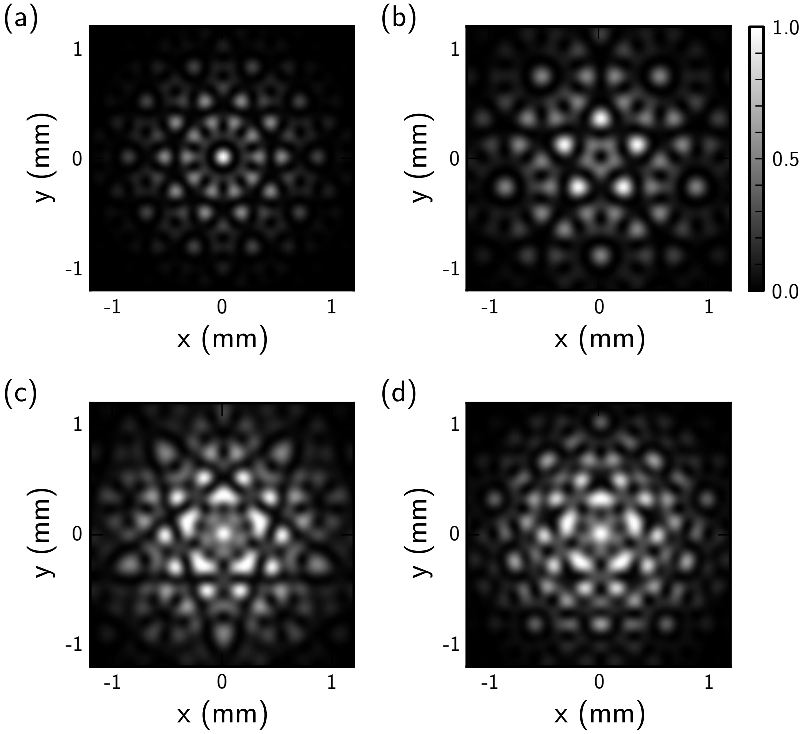

Figure 8.1: Diffraction patterns behind an $N = 5$ MPI. The parameters for the MPI are the same for all four images, but the wavelength of the light is varied. (a) $\lambda = 633$ nm with $\ell = 0$, (b) $\lambda = 780$ nm with $\ell = -1$, (c) a superposition of (a) and (b), and (d) a superposition of (a) and $\lambda = 700$ nm with $\ell = -1$.

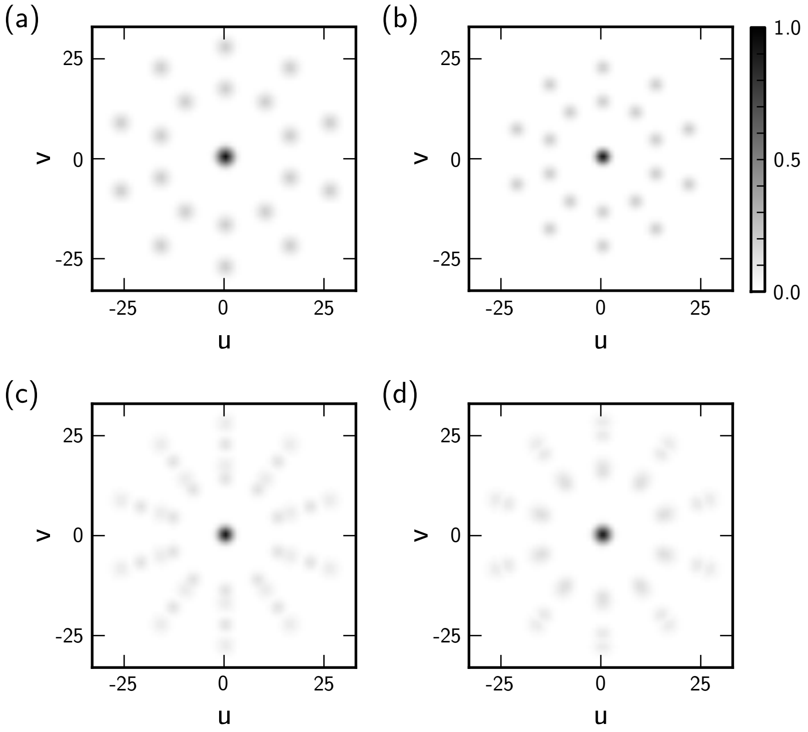

Figure 8.2: Absolute value of the numerical Fourier transform of the diffraction patterns shown in figure 8.1.

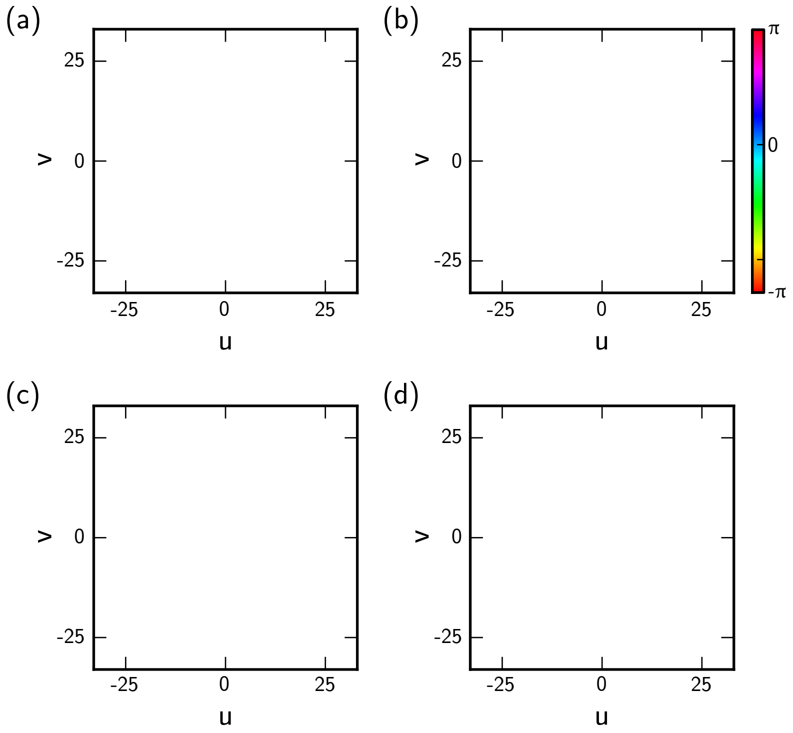

Figure 8.3: Phase of the numerical Fourier transform of the diffraction patterns shown in figure 8.1.

Figure 8.3 shows the phase of the Fourier transform and illustrates the overlap even better. One can clearly see that the phase is equal at all the pinholes for figure 8.3 (a) and increases from 0 to 2π in figure 8.3 (b). In figure 8.3 (c), one can still distinguish the two different wavelengths, but this is impossible in figure 8.3 (d), where the different pinholes overlap and the phase is blurred.

It depends on the exact source that is studied, how stringent the requirement on the wavelength is. If the source emits a spectrum that consists of several frequency lines that are not related, the vorticity can only be determined if the resulting peaks in the Fourier transform do not overlap. The required wavelength separation is then given by

$$\frac{\Delta\lambda}{\lambda} = \frac{2b}{4a\sin(\pi/N) - b}. \tag{8.4}$$

The size of the pinholes should be kept as small as possible to allow for a large wavelength range to be detectable. If the MPI is illuminated by a spectrum of different wavelengths, the analysis will return a blurred Fourier transformed image. If all different wavelengths contain a vortex, or in other words, if the input field is a white light vortex [77], the analysis will still return this vorticity and the method is adequate. In other cases, one has to be careful in interpreting the image.

8.2.2 Partial coherence

As mentioned before, it has been show that partially coherent light can still contain optical vortices and possess orbital angular momentum [72–76]. The aim of this section is to find out if an MPI is able to detect the vorticity in such a field. Intuitively, one would think that this is not the case, since the interference patterns is washed out by the (partial) incoherent character of the beam. However, Gbur *et al.* show that special types of partially coherent beams can generate diffraction patterns with true intensity zeroes [18]. Below we give an analysis that is based on the one presented by Gbur, but for a single wavelength. The interference pattern behind N pinholes is given by

$$I(x,y) \propto \mathbf{r}^{(N)\dagger}\mathbf{M}^{(N)}\mathbf{r}^{(N)}, \tag{8.5}$$

where

$$\mathbf{r}^{(N)} = \begin{pmatrix} A_1 e^{i\phi_1} \\ A_2 e^{i\phi_2} \\ \cdots \\ A_N e^{i\phi_N} \end{pmatrix}, \tag{8.6}$$

with A_j the amplitude of the optical field at the j-th pinhole and $\phi_j \equiv kR_j$ is the phase introduced by the distance R_j between the pinhole and the observation point (x,y). The matrix $\mathbf{M}^{(N)}$ is given by

$$\mathbf{M}^{(N)} = \begin{pmatrix} 1 & \mu_{12} & \cdots & \mu_{1N} \\ \mu_{12}^* & 1 & \cdots & \mu_{2N} \\ \vdots & \vdots & \ddots & \vdots \\ \mu_{1N}^* & \mu_{2N}^* & \cdots & 1 \end{pmatrix}, \tag{8.7}$$

where

$$\mu_{jk} = \frac{\langle A_j^* A_k \rangle}{\sqrt{I_j I_k}} \tag{8.8}$$

is the spectral degree of coherence and I_j would be the intensity observed if only the j-th pinhole would be open and the average is taken over an ensemble of space–frequency realizations of the field. The important parameter is the matrix $\mathbf{M}^{(N)}$, which describes the degree of coherence between each of the pinholes. The case of fully coherent beams, i.e. $\mu_{jk} = 1$ for all j,k has been described extensively in previous chapters. If not all μ_{jk} are equal to 1, the diffraction pattern will be partly washed out. In the case $N = 2$, this results in a pattern that does not contain any intensity zeroes. Gbur shows that for $N > 2$ and special classes of partially coherent beams, the intensity patterns will still contain

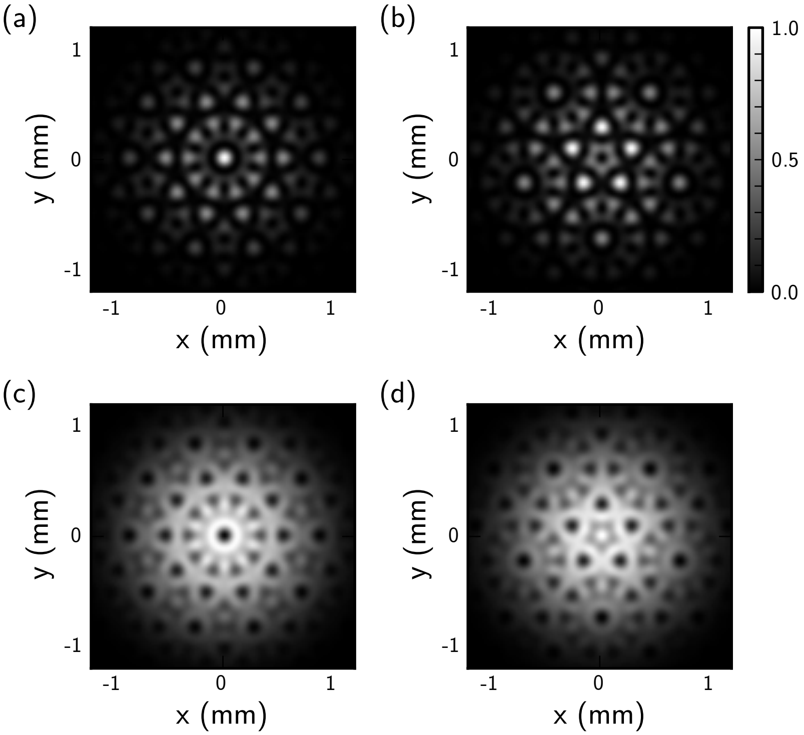

Figure 8.4: Diffraction patterns behind an $N = 5$ MPI for different types of input beams. (a) Coherent beam $l = 0$, (b) coherent beam $\ell = -1$, partially incoherent beam $\ell = 0$ satisfying equation 8.9 and (d) partially incoherent beam $\ell = -1$ satisfying equation 8.9. All other parameters are equal for all images.

intensity zeroes. One of these special cases is the case where all μ_{jk} are real and equal for $j \neq k$ and $\mu_{jj} = 1$ and

$$\mu = -\frac{1}{N-1}. \tag{8.9}$$

By comparing the diffraction patterns with the diffraction patterns obtained in previous chapters, one can see that these patterns are in fact equal, but with the colours inverted (see figure 8.4).

We also study intermediate cases by varying μ between 1 and $-\frac{1}{N-1}$. Figure 8.5 shows diffraction patterns for several values of μ. We believe that it is justified to conclude that, except for the fully incoherent case, all patterns contain a remainder of the pattern for the fully coherent case. This can be understood by the idea that a partially coherent beam can be considered as having a fully coherent part and a fully incoherent part. The fully coherent part will result in a diffraction pattern as studied in chapter 2 and the incoherent part will result in a uniform background. Applying the Fourier analysis, as described before, shows that this idea is justified. The Fourier transformed images are

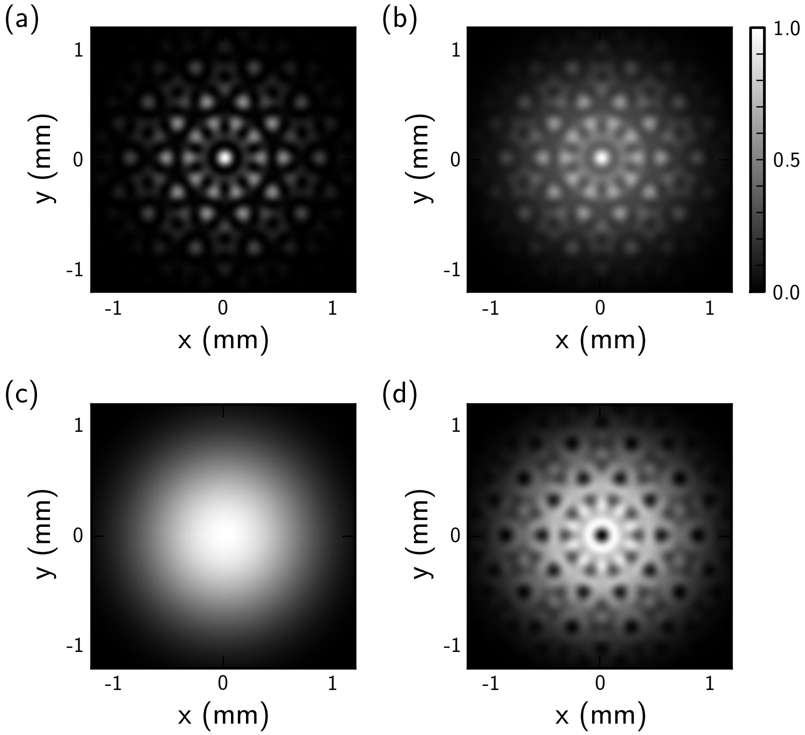

Figure 8.5: Diffraction patterns behind an $N = 5$ MPI for beams with different coherence. (a) Fully coherent beam $\mu = 1$, (b) $\mu = \frac{1}{N-1}$, (c) incoherent beam $\mu = 0$ and (d) $\mu = -\frac{1}{N-1}$. All other parameters are equal for all images.

comparable to the ones presented, for instance, in figure 8.2 and 8.3 (a) and (b), the only noticeable difference being that the central pixel has a larger amplitude due to the fact that all incoherent contributions end up in this pixel. The only exception is the case that $\mu_{jk} = 0$, or, in other words, the case of fully incoherent light, where the diffraction pattern is completely washed out.

8.3 Mode sorter

8.3.1 Monochromaticity

The OAM mode sorter that is extensively described in chapters 6 and 7 separates optical vortex states by transforming them to inclined plane waves, which are in turn focussed to different positions on a detector by a standard lens. The two custom optical elements that are needed to perform the transformation are created using two spatial light modulators (SLMs). The main advantage of SLMs is their flexibility to add any desired phase profile to an incoming beam. The phase profiles of the aforementioned custom optical components are described by (see chapter 6)

$$\begin{aligned}\phi_1(x,y) &= \frac{2\pi a}{\lambda f}\left[y \arctan\left(\frac{y}{x}\right) - x \ln\left(\frac{\sqrt{x^2+y^2}}{b}\right) + x\right], && (8.10)\\ \phi_2(u,v) &= -\frac{2\pi ab}{\lambda f} \exp\left(-\frac{u}{a}\right) \cos\left(\frac{v}{a}\right). && (8.11)\end{aligned}$$

In addition, the SLMs can be used to compensate for any aberrations or misalignment in the optical setup. The SLMs used in chapter 6 and 7 are reflective devices and their main disadvantage is their low reflectivity. Especially when combined with the beam splitters, that are used to ensure perpendicular incidence on the SLMs, the overall throughput of the mode sorter is low, typically about 1%. An alternative is to make the two custom components out of a transparent material like glass or plastic. The thickness profiles of the optical components then needs to be of the following form

$$\begin{aligned}t_1(x,y) &= \frac{\lambda \phi_1(x,y)}{2\pi(n-1)}, && (8.12)\\ t_2(u,v) &= \frac{\lambda \phi_2(u,v)}{2\pi(n-1)}, && (8.13)\end{aligned}$$

where n is the refractive index of the material. In other words

$$\begin{aligned}t_1(x,y) &= \frac{a}{f(n-1)}\left[y \arctan\left(\frac{y}{x}\right) - x \ln\left(\frac{\sqrt{x^2+y^2}}{b}\right) + x\right], && (8.14)\\ t_2(u,v) &= -\frac{ab}{f(n-1)} \exp\left(-\frac{u}{a}\right) \cos\left(\frac{v}{a}\right). && (8.15)\end{aligned}$$

Conveniently, these thickness profiles are independent of the wavelength of the input light, provided that the dispersion of the glass is negligible, which can be achieved with special types of glass over a fairly large range of wavelengths. The fact that the optics can operate at different wavelengths makes them extremely suitable for applications in high-dimensional optical communication.

8.3.2 Partial coherence

The orbital angular momentum of partially coherent light is still well defined and each photon has a well defined orbital angular momentum when measured. Since the mode sorter focusses individual photons to a position on the detector depending on the orbital angular momentum of the photon, the mode sorter still works for partially coherent light. The mode sorter can therefore be used to measure OAM spectrum of a partially coherent light beam.

8.3.3 Orthogonality

One disadvantage of the OAM mode sorter is the fact that the spatially separated output spots slightly overlap for different OAM states. In this section we further study this lack of orthogonality or separability, which introduces cross-talk between the states.

In the mode sorter based on spatial light modulators that is described in chapter 6 and 7, the output aperture of the mode sorter is square and completely filled by the transformed beam. As explained in chapter 7, there is no information about the OAM state in the one of the two transformed axes, so we will treat this problem as being one-dimensional. If we assume that the lens that focusses the transformed OAM states is much larger than the output aperture of the mode sorter, the focussed spots will have a intensity profile, $I(\alpha)$, determined by this square aperture

$$I(\alpha) \propto \left(\frac{\sin(\alpha)}{\alpha}\right)^2, \tag{8.16}$$

where $\alpha = \frac{kd}{2f}(t - t_\ell)$, $k = \frac{2\pi}{\lambda}$ is the wavenumber, λ the wavelength, d the aperture size, f the focal length and $t_\ell = \frac{\lambda f}{d}$ is the central position of the ℓ-th peak. The focussed peaks will slightly overlap, which is inherent to the optical design. One could argue that increasing the size of the aperture d would decreases the width of the spots. This does however also decreases the separation between the spots and the overlap will remain the same. The same reasoning holds for changing the focal length of the final lens. To further support this argument we present a numerical study of this system.

The most convenient way to use a mode sorter in a communication scheme would be to define regions of interest in its focal plane. If a photon hits the detector in a specific region, we can link this position to an orbital angular momentum. We define the ℓ-th region such that its centre coincides with the peak position for the ℓ-th mode. The width of one region is given by the separation of the two peaks and so

$$t_\ell - \frac{\lambda f}{2d} < t \leq t_\ell + \frac{\lambda f}{2d}. \tag{8.17}$$

Since $\sin(\alpha)/\alpha$ cannot be integrated analytically, we numerically evaluate the problem. First of all, we calculate the intensity in each of the defined regions for an input beam with $\ell = 0$. About 80% of the intensity ends up in the correct beam while the other 20% is spread out over the other bins, mostly the neighbouring ones.

To determine whether the overlap indeed does not depend on f or on d, we have calculated the intensity in all regions for several values of these parameters. As expected there is indeed no dependence.

As shown in the previous chapter, the mode sorter is sensitive to superpositions of modes. In addition the relative phase between modes is preserved. This relative phase does, however, alter the exact intensity distribution and therefore the intensity recorded

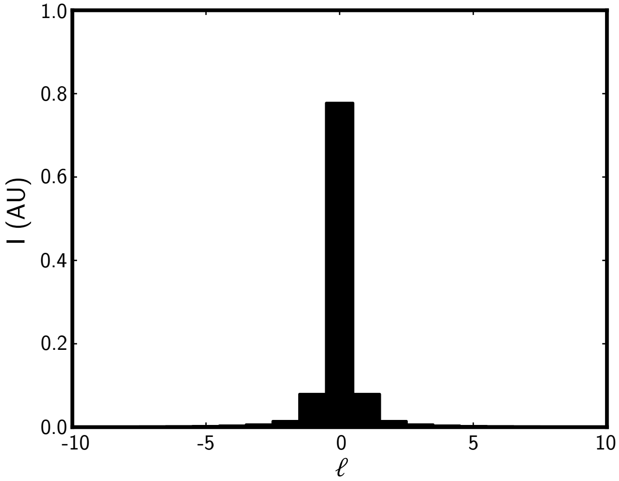

Figure 8.6: Intensity in each of the regions when illuminated with a pure $\ell = 0$ optical vortex.

in the defined bins. To study the effect of this relative phase, we have numerically studied an equal superposition of two modes, $\ell = -1$ and $\ell = 0$, where we vary the relative phase. Figure 8.7 shows the intensity in one of the regions, the one corresponding to either $\ell = -1$ or $\ell = 0$, which are equal since the problem is symmetric. As expected the intensity in the regions depends on the relative phase between the modes.

The variation is significant, about 20% of the peak value and this is something that needs to be taken into account, since it can affect the outcome of the measurements. The relative phase is also affected by the exact angular orientation of the mode sorter. A possible solution to this dependence on the relative phase is to use only pure modes and keep their relative phase fixed.

8.3.4 Quantum optics

Decreasing the intensity of the input beam does not change the working principle of the mode sorter and thus it should able to sort individual photons. The restriction that the spatially separated output spots slightly overlap leaves some inaccuracy in the determination of the OAM value of the photon. This can be resolved by modifying the optical design by adding a binary grating to the first optical element of the mode sorter and changing the second custom element accordingly. This will create a number of diffraction orders, all containing the same phase ramp. By changing the periodicity of the grating, these phase ramps can be connected to form a higher phase ramp, thereby increasing the separation between the final spots. Implementing this, does increase the overall optical complexity of the system.

In an optical communication scheme, one could also use only every second, third or even fourth mode. The latter option reduces the overlap between different output states

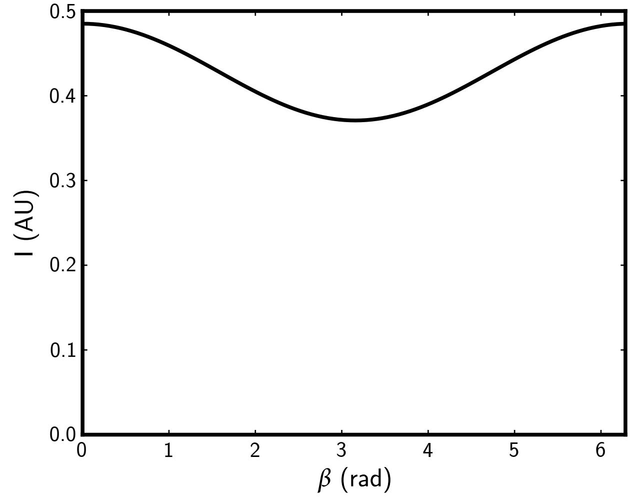

Figure 8.7: Intensity in the $\ell = 0$ region for an equal superposition of $\ell = -1$ and $\ell = 0$, $A \propto e^{-i\phi} + e^{i\beta}$ as a function of relative phase between the modes, β.

to below the 1% level.

As the orbital angular momentum states are spatially separated in the focus of the mode sorter, this allows us to perform operations on the individual modes in a spectrum, like changing the relative phase and amplitudes. This can also have applications in more fundamental studies of OAM.

One could use the same mode sorter, but inverted, to generate OAM states and superpositions thereof.

8.4 Conclusion

For almost twenty years, efficient measurement of the orbital angular momentum of light has been experimentally challenging. In this thesis we have presented two novel methods to solve this measurement problem, which open the way for use of the OAM of light in applications. These applications will bring new challenges like measuring the OAM of polychromatic and (partially) incoherent light. In this final chapter we have shown with some initial calculations that the multi-pinhole interferometer is able to detect the OAM of an incoming light beam with a limited wavelength range and that it still works for partially incoherent light. In addition, we have shown that the mode sorter works for both polychromatic and partially coherent light. Finally, we have shown that the inherent cross-talk in the mode sorter can be reduced by changing the optical design. All these aspects of the applications of orbital angular momentum detection are very interesting and the initial calculations presented here can serve as a starting point for more detailed study.

Bibliography

[1] L. Allen, M. W. Beijersbergen, R. J. C. Spreeuw, and J. P. Woerdman, *Orbital angular momentum of light and the transformation of laguerre-gaussian laser modes,* Phys. Rev. A **45**, 8185 (1992).

[2] G. Molina-Terriza, J. P. Torres, and L. Torner, *Twisted photons,* Nature Phys. **3**, 305 (2007).

[3] R. A. Beth, *Mechanical detection and measurement of the angular momentum of light,* Phys. Rev. **50**, 115 (1936).

[4] H. He, M. E. J. Friese, N. R. Heckenberg, and H. Rubinsztein-Dunlop, *Direct observation of transfer of angular momentum to absorptive particles from a laser beam with a phase singularity,* Phys. Rev. Lett. **75**, 826 (1995).

[5] M. W. Beijersbergen, R. P. C. Coerwinkel, M. Kristensen, and J. P. Woerdman, *Helical-wavefront laser beams produced with a spiral phase plate,* Opt. Commun. **112**, 321 (1994).

[6] I. V. Basistiy, M. S. Soskin, and M. V. Vasnetsov, *Optical wavefront dislocations and their properties,* Opt. Commun. **119**, 604 (1995).

[7] G. F. Brand, *Phase singularities in beams,* Am. J. Phys. **67**, 55 (1999).

[8] N. B. Baranova, B. Ya. Zel'dovich, A. V. Mamaev, N. F. Pilipetskii, and V. V. Shkukov, *Dislocations of the wavefront of a speckle-inhomogeneous field (theory and experiment),* JETP Lett. **33**, 195 (1981).

[9] I. Freund, *Optical vortices in gaussian random wave fields: statistical probability densities,* J. Opt. Soc. Am. A **11**, 1644 (1994).

[10] J. F. Nye and M. V. Berry, *Dislocations in wave trains,* Proc. R. Soc. Lond. A **336**, 165 (1974).

[11] M. Harwit, *Photon orbital angular momentum in astrophysics,* Astrophys. J. **597**, 1266 (2003).

[12] B. Thidé, H. Then, J. Sjöholm, K. Palmer, J. Bergman, T. D. Carozzi, Ya. N. Istomin, N. H. Ibragimov, and R. Khamitova, *Utilization of photon orbital angular momentum in the low-frequency radio domain,* Phys. Rev. Lett. **99**, 087701 (2007).

[13] J. Leach, M. J. Padgett, S. M. Barnett, S. Franke-Arnold, and J. Courtial, *Measuring the orbital angular momentum of a single photon,* Phys. Rev. Lett. **88**, 257901 (2002).

[14] M. Harris, C. A. Hill, P. R. Tapster, and J. M. Vaughan, *Laser modes with helical wave fronts,* Phys. Rev. A **49**, 3119 (1994).

[15] M. Padgett, J. Arlt, N. Simpson, and L. Allen, *An experiment to observe the intensity and phase structure of laguerre-gaussian laser modes,* Am. J. Phys. **64**, 77 (1996).

[16] T. Young, *An account of some cases of the production of colours, not hitherto described,* Philos. Trans. R. Soc. Lond. **92**, 387 (1802).

[17] H. I. Sztul and R. R. Alfano, *Double-slit interference with laguerre-gaussian beams,* Opt. Lett. **31**, 999 (2006).

[18] G. Gbur, T. D. Visser, and E. Wolf, *Complete destructive interference of partially coherent fields,* Opt. Commun. **239**, 15 (2004).

[19] C. H. Gan and G. Gbur, *Phase and coherence singularities generated by the interference of partially coherent fields,* Opt. Commun. **280**, 249 (2007).

[20] C. S. Cockell, A. Léger, M. Fridlund, T. M. Herbst, L. Kaltenegger, O. Absil, C. Beichman, W. Benz, M. Blanc, A. Brack, A. Chelli, L. Colangeli, H. Cottin, F. Coudé du Foresto, W. C. Danchi, D. Defrère, J.-W. den Herder, C. Eiroa, J. Greaves, T. Henning, K. J. Johnston, H. Jones, L. Labadie, H. Lammer, R. Launhardt, P. Lawson, O. P. Lay, J.-M. LeDuigou, R. Liseau, F. Malbet, S. R. Martin, D. Mawet, D. Mourard, C. Moutou, L. M. Mugnier, M. Ollivier, F. Paresce, A. Quirrenbach, Y. D. Rabbia, J. A. Raven, H. J. A. Rottgering, D. Rouan, N. C. Santos, F. Selsis, E. Serabyn, H. Shibai, M. Tamura, E. Thiébaut, F. Westall, and G. J. White, *Darwin - a mission to detect and search for life on extrasolar planets,* Astrobiol. **9**, 1 (2009).

[21] G. Foo, D. M. Palacios, and G. A. Swartzlander, Jr., *Optical vortex coronagraph,* Opt. Lett. **30**, 3308 (2005).

[22] European Southern Observatory Very Large Telescope.

[23] European Southern Observatory Atacama Large Millimeter/submillimeter Array.

[24] F. Vakili, A. Belu, E. Aristidi, E. Fossat, A. Maillard, L. Abe, K. Agabi, J. Vernin, J. B. Daban, W. Hertmanni, F.-X. Schmider, P. Assus, V. Coudé du Foresto, and M. R. Swain, *Keops: Kiloparsec explorer for optical planet search, a direct-imaging optical array at dome c of antarctica,* Proc. SPIE **5491**, 1580 (2004).

[25] S. Franke-Arnold, L. Allen, and M. Padgett, *Advances in optical angular momentum,* Laser Photon. Rev. **2**, 299 (2008).

[26] N. M. Elias II, *Photon orbital angular momentum in astronomy,* Astron. Astrophys. **492**, 883 (2008).

[27] G. C. G. Berkhout and M. W. Beijersbergen, *Method for probing the orbital angular momentum of optical vortices in electromagnetic waves from astronomical objects,* Phys. Rev. Lett. **101**, 100801 (2008).

[28] K. O'Holleran, M. R. Dennis, F. Flossmann, and M. J. Padgett, *Fractality of light's darkness,* Phys. Rev. Lett. **100**, 053902 (2008).

[29] A. Mair, A. Vaziri, G. Weihs, and A. Zeilinger, *Entanglement of the orbital angular momentum states of photons,* Nature **412**, 313 (2001).

[30] G. Molina-Terriza, J. P. Torres, and L. Torner, *Management of the angular momentum of light: preparation of photons in multidimensional vector states of angular momentum,* Phys. Rev. Lett. **88**, 013601 (2001).

[31] F. S. Roux, *Coupling of noncanonical optical vortices,* J. Opt. Soc. Am. B **21**, 664 (2004).

[32] M. R. Dennis, *Local phase structure of wave dislocation lines: twist and twirl,* J. Opt. A **6**, S202 (2004).

[33] G. Gibson, J. Courtial, M. J. Padgett, M. Vasnetsov, V. Pas'ko, S. M. Barnett, and S. Franke-Arnold, *Free-space information transfer using light beams carrying orbital angular momentum,* Opt Express **12**, 5448 (2004).

[34] J. W. Goodman, *Some fundamental properties of speckle,* J. Opt. Soc. Am. **66**, 1145 (1976).

[35] J. W. Goodman, *Speckle phenomena in optics* (Roberts & Company, Englewood, 2006).

[36] I. Freund, N. Shvartsman, and V. Freilikher, *Optical dislocation networks in highly random media,* Opt. Commun. **101**, 247 (1993).

[37] D. Rozas, C. T. Law, and G. A. Swartzlander, Jr., *Propagation dynamics of optical vortices,* J. Opt. Soc. Am. B **14**, 3054 (1997).

[38] W. Wang, N. Ishii, S. G. Hanson, Y. Miyamoto, and M. Takeda, *Phase singularities in analytic signal of white-light speckle pattern with application to micro-displacement measurement,* Opt. Commun. **248**, 59 (2005).

[39] D. L. Fried and J. L. Vaughn, *Branch cuts in the phase function,* Appl. Opt. **31**, 2865 (1992).

[40] D. L. Fried, *Branch point problem in adaptive optics,* J. Opt. Soc. Am. A **15**, 2759 (1998).

[41] C.-S. Guo, S.-J. Yue, and G.-X. Wei, *Measuring the orbital angular momentum of optical vortices using a multipinhole plate,* Appl. Phys. Lett. **94**, 231104 (2009).

[42] R. W. Schoonover and T. D. Visser, *Creating polarization singularities with an n-pinhole interferometer,* Phys. Rev. A **79**, 043809 (2009).

[43] G. C. G. Berkhout and M. W. Beijersbergen, *Using a multipoint interferometer to measure the orbital angular momentum of light in astrophysics,* J. Opt. A **11**, 094021 (2009).

[44] M. R. Dennis, *Topological singularities in wave fields*, Ph.D. thesis, University of Bristol (2001).

[45] Y. Y. Schechner and J. Shamir, *Parameterization and orbital angular momentum of anisotropic dislocations,* J. Opt. Soc. Am. A **13**, 967 (1996).

[46] M. V. Berry and M. R. Dennis, *Phase singularities in isotropic random waves,* Proc. R. Soc. Lond. A **456**, 2059 (2000).

[47] J. Leach, M. R. Dennis, J. Courtial, and M. J. Padgett, *Vortex knots in light,* New. J. Phys. **7**, 55 (2005).

[48] N. Bloembergen, *Conservation laws in nonlinear optics,* J. Opt. Soc. Am. **70**, 1429 (1980).

[49] A. Vaziri, G. Weihs, and A. Zeilinger, *Experimental two-photon, three-dimensional entanglement for quantum communication,* Phys. Rev. Lett. **89**, 240401 (2002).

[50] J. T. Barreiro, T.-C. Wei, and P. G. Kwiat, *Beating the channel capacity limit for linear photonic superdense coding,* Nature Phys. **4**, 282 (2008).

[51] J. Leach, B. Jack, J. Romero, A. K. Jha, A. M. Yao, S. Franke-Arnold, D. G. Ireland, R. W. Boyd, S. M. Barnett, and M. J. Padgett, *Quantum correlations in optical angle-orbital angular momentum variables,* Science **329**, 662 (2010).

[52] V. Yu. Bazhenov, M. S. Soskin, and M. V. Vasnetsov, *Screw dislocations in light wavefronts,* J. Mod. Opt. **39**, 985 (1992).

[53] N. R. Heckenberg, R. McDuff, C. P. Smith, H. Rubinsztein-Dunlop, and M. J. Wegener, *Laser beams with phase singularities,* Opt. Quantum Electron. **24**, S951 (1992).

[54] S. N. Khonina, V. V. Kotlyar, R. V. Skidanov, V. A. Soifer, P. Laakkonen, and J. Turunen, *Gauss-laguerre modes with different indices in prescribed diffraction orders of a diffractive phase element,* Opt. Commun. **175**, 301 (2000).

[55] J. M. Hickmann, E. J. S. Fonseca, W. C. Soares, and S. Chávez-Cerda, *Unveiling a truncated optical lattice associated with a triangular aperture using light's orbital angular momentum,* Phys. Rev. Lett. **105**, 053904 (2010).

[56] J. Courtial, D. A. Robertson, K. Dholakia, L. Allen, and M. J. Padgett, *Rotational frequency shift of a light beam,* Phys. Rev. Lett. **81**, 4828 (1998).

[57] O. Bryngdahl, *Geometrical transformations in optics,* J. Opt. Soc. Am. **64**, 1092 (1974).

[58] Y. Saito, S.-I. Komatsu, and H. Ohzu, *Scale and rotation invariant real time optical correlator using computer generated hologram,* Opt. Commun. **47**, 8 (1983).

[59] W. J. Hossack, A. M. Darling, and A. Dahdouh, *Coordinate transformations with multiple computer-generated optical elements,* J. Mod. Opt. **34**, 1235 (1987).

[60] C. E. Shannon, *A mathematical theory of communication,* Bell Syst. Tech. J. **27**, 623 (1948).

[61] M. J. Padgett and L. Allen, *The poynting vector in laguerre-gaussian laser modes,* Opt. Commun. **121**, 36 (1995).

[62] S. Furhapter, A. Jesacher, S. Bernet, and M. Ritsch-Marte, *Spiral phase contrast imaging in microscopy,* Opt. Express **13**, 689 (2005).

[63] M. W. Beijersbergen, L. Allen, H. E. L. O. van der Veen, and J. P. Woerdman, *Astigmatic laser mode converters and transfer of orbital angular-momentum,* Opt. Commun. **96**, 123 (1993).

[64] J. Nye, *Natural focusing and fine structure of light* (Institute of Physics Publishing, Bristol, 1999).

[65] E. Nagali, F. Sciarrino, F. De Martini, B. Piccirillo, E. Karimi, L. Marrucci, and E. Santamato, *Polarization control of single photon quantum orbital angular momentum states,* Opt. Express **17**, 18745 (2009).

[66] G. C. G. Berkhout, M. P. J. Lavery, J. Courtial, M. W. Beijersbergen, and M. J. Padgett, *Efficient sorting of orbital angular momentum states of light,* Phys. Rev. Lett. **105**, 153601 (2010).

[67] H. Di Lorenzo Pires, H. C. B. Florijn, and M. P. van Exter, *Measurement of the spiral spectrum*

of entangled two-photon states, Phys. Rev. Lett. **104**, 020505 (2010).

[68] S. S. R. Oemrawsingh, E. R. Eliel, G. Nienhuis, and J. P. Woerdman, *Intrinsic orbital angular momentum of paraxial beams with off-axis imprinted vortices,* J. Opt. Soc. Am. A **21**, 2089 (2004).

[69] J. B. Pors, A. Aiello, S. S. R. Oemrawsingh, M. P. van Exter, E. R. Eliel, and J. P. Woerdman, *Angular phase-plate analyzers for measuring the dimensionality of multimode fields,* Phys. Rev. A **77**, 033845 (2008).

[70] M. V. Vasnetsov, V. A. Pas'ko, and M. S. Soskin, *Analysis of orbital angular momentum of a misaligned optical beam,* New J. Phys. **7**, 46 (2005).

[71] F. Tamburini, B. Thidé, G. Molina-Terriza, and G. Anzolin, *Twisting of light around rotating black holes,* Nature Phys. **7**, 195 (2011).

[72] G. S. Agarwal, *Su(2) structure of the poincaré sphere for light beams with orbital angular momentum,* J. Opt. Soc. Am. A **16**, 2914 (1999).

[73] J. Serna and J. M. Movilla, *Orbital angular momentum of partially coherent beams,* Opt. Lett. **26**, 405 (2001).

[74] S. A. Ponomarenko, *A class of partially coherent beams carrying optical vortices,* J. Opt. Soc. Am. A **18**, 150 (2001).

[75] G. V. Bogatyryova, C. V. Fel'de, P. V. Polyanskii, S. A. Ponomarenko, M. S. Soskin, and E. Wolf, *Partially coherent vortex beams with a separable phase,* Opt. Lett. **28**, 878 (2003).

[76] H. Di Lorenzo Pires, J. Woudenberg, and M. P. van Exter, *Measurement of the orbital angular momentum spectrum of partially coherent beams,* Opt. Lett. **35**, 889 (2010).

[77] J. Leach and M. J. Padgett, *Observation of chromatic effects near a white-light vortex,* New J. Phys. **5**, 154 (2003).

Samenvatting

Licht is een veelvoorkomende drager van informatie. De intensiteit, richting, kleur en polarisatie geven informatie over de bron van het licht en het medium waar het doorheen is gegaan. Door middel van fotodetectoren, camera's, spectrometers en polarisatoren kunnen deze eigenschappen nauwkeurig worden gemeten. Op deze manier kan niet alleen kennis worden vergaard over de bron en het medium; ook kan het licht worden gebruikt om informatie te versturen van de ene plek naar de andere, door deze informatie te versleutelen in één of meerdere eigenschappen van het licht.

In de afgelopen twintig jaar is de interesse gegroeid voor een andere eigenschap van licht, het baanimpulsmoment. In tegenstelling tot de polarisatie, die twee toestanden, horizontaal en verticaal, kan aannemen, kan het baanimpulsmoment van een lichtbundel oneindig veel orthogonale toestanden aannemen. Als deze eigenschap nauwkeurig kan worden gemeten, dan biedt dit mogelijkheden voor interessant, nieuw onderzoek en kan het baanimpulsmoment worden gebruikt als extra eigenschap om informatie in te versleutelen, waarbij het aftelbaar oneindige mogelijke toestanden een groot voordeel is.

Eén manier om licht met baanimpulsmoment te maken is door middel van zogenaamde Laguerre-Gauss bundels. Deze bundels hebben een fasesingulariteit waaromheen de fase van het optische veld lineair toeneemt met de poolhoek ϕ volgens $\exp(i\ell\phi)$, waarbij ℓ een geheel getal is; in het centrum van zo een bundel bevindt zich een zogenaamde optische vortex. Op de positie van de fasesingulariteit is de intensiteit gelijk aan nul en, in het geval van een Laguerre-Gauss bundel resulteert dit in een ringvorming intensiteitsprofiel. Elk foton in een Laguerre-Gauss bundel heeft een baanimpulsmoment van $\ell\hbar$. ℓ wordt vaak ook gebruikt om de topologische lading van de optische vortex aan te geven. $\ell = 0$ komt overeen met een vlak faseprofiel, waarvan het verre veld van een puntbron, zoals bijvoorbeeld een ster, een veelvoorkomend voorbeeld is. Bundels met een optische vortex kunnen worden gemaakt met speciale optische elementen, zoals een spiraalfaseplaat, een vorkhologram of een *spatial light modulator*. Op deze manier kan een groot aantal verschillende waarden van ℓ worden bereikt. Optische vortices komen ook voor als hogere orde toestanden van laser licht, in optische caustieken en in spikkelpatronen.

Het meten van het baanimpulsmoment van licht zonder kennis vooraf is erg uitdagend. Een ideaal meetsysteem zou, in principe, oneindig veel verschillende uitgangen moeten hebben, elk overeenkomend met één van de baanimpulsmomenttoestanden. Zo een systeem zou het complexe equivalent zijn van een polariserende bundelsplitser, die twee uitgangen heeft, elk overeenkomend met één van de twee polarisatietiestanden. Een alternatief om de polarisatie van licht te bepalen is het gebruik van een polarisator, die één van de toestanden blokkeert en de ander doorlaat, hetgeen we een filter noemen.

In het verleden zijn verschillende manieren bestudeerd om het baanimpulsmoment van licht te meten. Het interfereren van een optische vortex met een bundel met een vlak faseprofiel resulteert in een interferentiepatroon waaruit de topologische lading van de vortex kan worden bepaald. Het feit dat er een tweede bundel nodig is, maakt deze methode niet erg geschikt voor sommige toepassingen, met name als de bestudeerde bundel groot is in vergelijking met een typische detector, zoals bijvoorbeeld te verwachten is voor licht van astronomische bronnen. Een filter voor baanimpulsmomenttoestanden kan worden gerealiseerd met een spiraalfaseplaat, die kan worden gebruikt om te testen of een foton zich in een bepaalde toestand bevindt of niet. Tenslotte kan een combinatie van Mach-Zehnder interferometers en Dove prisma's worden gebruikt om de baanimpulsmomenttoestand van een foton te meten, maar dit is technisch erg uitdagend en moeilijk in te bouwen in een groter optisch systeem.

In dit proefschrift presenteren we twee nieuwe manieren om het baanimpulsmoment van licht te meten. De eerste manier, waarvan we de details in hoofdstuk 2 en 3 beschrijven, is gebaseerd op een meerpuntsinterferometer, een systeem van een aantal openingen in een cirkelvormig patroon, waarachter het licht via diffractie wordt gecombineerd. We laten zien dat de topologische lading van een inkomende optische vortex kan worden bepaald op basis van de interferentiepatronen achter zo een meerpuntsinterferometer. Het grootste voordeel van een meerpuntsinterferometer is het feit dat de openingen ver van elkaar kunnen worden geplaatst, hetgeen het mogelijk maakt om dit systeem aan te passen aan optische bundels of velden die veel groter zijn dan een typische detector. De meerpuntsinterferometer kan ook worden gebruikt om zogenaamde vortexkaarten te maken, op basis waarvan het mogelijk is om optische vortices in een spikkelpatroon te vinden, hetgeen het onderwerp is van hoofdstuk 4 en 5.

In hoofdstuk 6 presenteren we een toestandssorteerder voor baanimpulsmomenttoestanden. De toestandssorteerder bestaat uit twee speciale optische elementen en twee lenzen die inkomende optische vortices met een verschillende topologische lading omvormen en focusseren op verschillende posities op een detector. In hoofdstuk 7 laten we zien dat deze toestandssorteerder ook in staat is om de bijdragen van verschillende optische vortices in een superpositie te bepalen. In speciale gevallen kunnen we zelfs de relatieve fase tussen de toestanden bepalen.

Alle resultaten in hoofdstuk 2 tot en met 7 zijn verkregen met monochromatisch en coherent licht. In hoofdstuk 8 breiden we deze resultaten theoretisch uit naar polychromatisch en (deels) incoherent licht. De resultaten van deze berekeningen dienen als uitgangspunt bij het bestuderen van toepassingen van het baanimpulsmoment van licht, zoals bijvoorbeeld optische communicatie.

Curriculum Vitae

Gregorius Cornelis Gerardus (Joris) Berkhout was born on 14 January 1983 in Beverwijk, The Netherlands. He attended the Augustinus College in Beverwijk from 1995 to 2001, after which he enrolled in the physics programme at Leiden University. Within this programme, he performed a research project in the Molecular Nano-Optics and Spins (MoNOS) group at Leiden University on the dynamics of single fluorescent molecules in glycerol at low temperatures, supervised by dr. Rob Zondervan and prof. dr. Michel Orrit. He further did an internship at cosine BV under supervision of dr. Stefan Kraft and prof. dr. Marco Beijersbergen, working on the development of a test bench for the adaptive optics facility of the European Southern Observatory's Very Large Telescope. In 2007 he received his master's degree in physics. During the course of his study, he was an active member of the society for physics, astronomy, mathematics and computer science students, De Leidsche Flesch, and served as the student member of the board of the Faculty of Science at Leiden University, in which capacity he was responsible for all student affairs at the faculty.

In 2007, Joris started working as a PhD student with prof. dr. Marco Beijersbergen, spending part of his time in the Quantum Optics group at Leiden University and part of his time at cosine BV. His research focussed on finding methods to measure the orbital angular momentum of light, the results of which are presented in this thesis. Part of this research was performed during a five month visit to the Optics group of prof. dr. Miles Padgett at the University of Glasgow. At cosine BV, he further worked on the design and testing of liquid crystal based programmable optical elements. Within this project he was responsible for part of the technical work as well as for the project management. During the course of his PhD, he was a member of the Casimir PhD platform and helped organize the biannual Casimir spring school. He supervised a master student, was teaching assistant for the bachelor course on electromagnetism, and organized a workshop on the design of instruments for space applications. He presented his work at several international conferences. With his contribution to the Frontiers in Optics conference in 2010 in Rochester, NY, he won the Emil Wolf outstanding student paper competition.

List of publications

- R. Zondervan, F. Kulzer, G. C. G. Berkhout, and M. Orrit,
  Local viscosity of supercooled glycerol near T_g probed by rotational diffusion of ensembles and single dye molecules,
  Proceedings of the National Academy of Sciences of the United States of America **104**, 12628 (2007).

- G. C. G. Berkhout and M. W. Beijersbergen,
  Method for probing the orbital angular momentum of optical vortices in electromagnetic waves from astronomical objects,
  Physical Review Letters **101**, 100801 (2008).
  (*Chapter 2 of this thesis*)

- G. C. G. Berkhout and M. W. Beijersbergen,
  Using a multipoint interferometer to measure the orbital angular momentum of light in astrophysics,
  Journal of Optics A: Pure and Applied Optics **11**, 094021 (2009).
  (*Chapter 3 of this thesis*)

- G. C. G. Berkhout and M. W. Beijersbergen,
  Measuring optical vortices in a speckle pattern using a multi-pinhole interferometer,
  Optics Express **18**, 13836 (2010).
  (*Chapter 4 of this thesis*)

- G. C. G. Berkhout, M. P. J. Lavery, J. Courtial, M. W. Beijersbergen, and M. J. Padgett,
  Efficient sorting of orbital angular momentum states of light,
  Physical Review Letters **105**, 153601 (2010).
  (*Chapter 6 of this thesis*)

- M. P. J. Lavery, G. C. G. Berkhout, J. Courtial, and M. J. Padgett,
  Measurement of misaligned light beams carrying orbital angular momentum,
  Journal of Optics **13**, 064006 (2011).

- G. C. G. Berkhout, M. P. J. Lavery, M. J. Padgett, and M. W. Beijersbergen,
  Measuring orbital angular momentum superpositions of light by mode transformation,
  Optics Letters **36**, 1863 (2011).
  (*Chapter 7 of this thesis*)

- E. J. Buis, G. C. G. Berkhout, M. J. Collon, S. Hannemann, A. K. Kirby, G. D. Love, and J. M. Taylor,
  Proton irradiation of liquid crystal based adaptive optical devices,
  under review for Nuclear Instruments and Methods B.

- G. C. G. Berkhout, Y. O. van Boheemen, M. P. van Exter, and M. W. Beijersbergen
  Quantitative mapping of the optical vortices in a speckle pattern,
  in preparation for publication.
  (*Chapter 5 of this thesis*)

Nawoord

Met dit proefschrift sluit ik de interessante periode af die de afgelopen vier jaar voor me is geweest; een periode waarin ik niet alleen veel heb geleerd over het meten van het baanimpulsmoment van licht, maar ook een waarin ik de kans heb gekregen om mezelf op vele vlakken verder te ontwikkelen. Velen hebben bijgedragen aan deze ontwikkeling en een aantal van hen wil ik op deze plek in het bijzonder bedanken.

Allereerst wil ik mijn promotor, Marco Beijersbergen, bedanken voor de kans om te werken op het raakvlak van wetenschap en industrie en voor het mij bijbrengen van de projectmatige aanpak die zo goed bij dit type werk past.

I am very grateful to Miles Padgett for the opportunity to visit his group at the University of Glasgow and his help in finding a solution to our shared problem of measuring the orbital angular momentum of light. I would like to thank Martin Lavery for our fruitful collaboration and for making my time in Glasgow such a great one.

Ik wil Eric Eliel bedanken voor het stimuleren van de samenwerking met de Quantumoptica groep, Martin van Exter voor zijn gewaardeerde kritische blik op mijn werk en Yorick van Boheemen, zonder wiens inspanningen hoofdstuk 5 niet zo mooi zou zijn geworden als het nu is. Mijn tijd in de Quantumoptica groep zou niet zo aangenaam geweest zijn zonder alle collega's en in het bijzonder medepromovendi Eduard Driessen, Wouter Peeters, Bart-Jan Pors, Ljubisa Babic, Henrique di Lorenzo Pires, Philip Chimento en Frerik van Beijnum. Ik ben Arno van Amersfoort dankbaar voor de ondersteuning op technisch gebied en Henriëtte van Leeuwen voor de administratieve hulp.

Ik ben alle collega's en oud-collega's bij cosine buitengewoon dankbaar voor de mogelijkheid om te leren van de diversiteit in hun achtergronden en de projecten waar ze aan werken. In het bijzonder wil ik Max Collon bedanken voor zijn vertrouwen in mijn kwaliteiten als projectmanager en de mogelijkheid deze onder zijn hoede verder te ontwikkelen. Giuseppe Vacanti wil ik bedanken voor zijn nimmer aflatende enthousiasme over mijn werk en Ernst-Jan Buis voor de samenwerking op wetenschappelijk gebied, maar vooral voor zijn zo gewaardeerde andere kijk op zaken.

Bas, Marten, Pascal, Dave en Wouter, bedankt voor de afleiding op donderdagavond, die soms hard nodig, maar altijd welkom was. Martijn en Michiel ben ik dankbaar voor de vele gesprekken over werk, over privé en natuurlijk over ideeën om een eigen bedrijf te beginnen, hetgeen we in de toekomst hopelijk nog eens een gaan doen.

Mijn paranimfen, Maaike en Richard, wil ik bedanken voor de steun die ze, ieder op hun eigen manier, de afgelopen vier jaar voor me zijn geweest, tot en met de verdediging van dit proefschrift aan toe.

En tot slot wil ik mijn ouders bedanken, die me hebben geleerd hoe belangrijk het is om jezelf te ontwikkelen, hetgeen, onder andere, heeft geresulteerd in de totstandkoming van dit proefschrift.